Article

Hydrodynamic Features of an Undular Bore Traveling on a 1:20 Sloping Beach

Chang Lin [1],*, Wei-Ying Wong [1], Ming-Jer Kao [1], James Yang [2,3], Rajkumar V. Raikar [4] and Juan-Ming Yuan [5]

[1] Department of Civil Engineering, National Chung Hsing University, Taichung City 40227, Taiwan
[2] Vattenfall AB Research and Development, Älvkarleby Laboratory, SE-81426 Älvkarleby, Sweden
[3] Division of Concrete Structures, Royal Institute of Technology (KTH), SE-10044 Stockholm, Sweden
[4] Department of Civil Engineering, KLE Dr. M. S. Sheshgiri College of Engineering and Technology, Angol Main Road, Udyambag, Belgaum, Karnataka 590008, India
[5] Department of Data Science and Big Data Analytics, Providence University, Taichung City 43301, Taiwan
* Correspondence: chenglin@nchu.edu.tw; Tel.: +886-4-2285-5182

check for updates

Abstract: The hydrodynamic characteristics, including local and convective accelerations as well as pressure gradient in the horizontal direction, of the external stream of an undular bore propagating on a 1:20 sloping beach are experimentally studied. A bore with the water depth ratio of 1.70 was generated downstream of a suddenly lifted gate. A high-speed particle image velocimetry was employed to measure the velocity fields during the run-up and run-down motions. The time series of free surface elevation and velocity field/profile of the generated bore, comprising a pure bore accompanied by a series of dispersive leading waves, are first demonstrated. Based on the fast Fourier transform (FFT) and inverse FFT (IFFT) techniques, the free surface elevation of leading waves and the counterpart of pure bore are acquired separately at a specified measuring section (SMS), together with the uniform horizontal velocity of the pure bore. The effect of leading-wave-induced velocity shift on the velocity profiles of the generated bore are then evaluated at the SMS. To understand the calculation procedure of accelerations and pressure gradient, three tabulated forms are provided as illustrative examples. Accordingly, the relationships among the partially depth-averaged values of the non-dimensional local acceleration, convective acceleration, total acceleration and pressure gradient of the generated/pure bore acquired at the SMS versus the non-dimensional time are elucidated. The trends in the non-dimensional accelerations and pressure gradient of the external stream of generated bore are compared with those of the pure bore. During the run-up motion from the instant of arrival of the bore front to the moment of the peak level at the SMS, continuous decrease in the onshore uniform horizontal velocity, and successive deceleration of the pure bore in the onshore direction are evidenced, exhibiting the pure bore under the adverse pressure gradient with decreasing magnitude. However, the pure bore once ridden by the leading waves is decelerated/accelerated spatially and accelerated/decelerated temporally in the onshore direction during the rising/descending free surface of each leading wave. This fact highlights the effect of pre-passing/post-passing of the leading wave crest on the velocity distribution of generated bore. It is also found that, although the leading waves have minor contribution on the power spectrum of the free surface elevation as compared with that of the pure bore, the leading waves do play an important role on the magnitudes of both accelerations and pressure gradient. The largest magnitude of the acceleration contributed by the leading waves is around 26 times the counterpart contributed by the pure bore. Further, during the run-down motion right after the moment for the peak level of the bore, a linear increase in the magnitude of the offshore uniform horizontal velocity and a constant local acceleration with increasing time are both identified. The partially depth-averaged value of the non-dimensional pressure gradient is equal to a small negative constant (−0.0115) in the offshore direction, indicating that the bore is subject to a constant favorable pressure gradient.

1. Introduction

Tsunamis are a series of extremely long waves generated by disturbances associated primarily with earthquakes occurring below or near the ocean floor. They can travel across the ocean and cause serious disasters. As indicated by Grue et al. [1], a series of long waves, consisting of undular bores and solitary waves, were generated in the Strait of Malacca by the 26 December 2004 causing the Indian Ocean Tsunami. These disasters caused by tsunamis have received much attention, especially after the great earthquakes taking place in Indonesia in 2004 and 2018 as well as in Japan in 2011. Most of the damages are related to the run-up and run-down motions of the long waves, which inundates inland and backwashes seawards in the coastal zones. Thus, understanding the features of the long-wave-induced flow field during the whole process is very important for planning and decision making associated with the safeguarding of coastal areas, designs of warning systems, and effective evacuation procedures.

This study, an extension of Lin et al. [2], aims to elucidate the characteristics of the local and convective accelerations as well as the pressure gradient of the external stream of an undular bore, propagating on a 1:20 sloping beach. Previous literatures are briefly reviewed in the following.

With a series of experiments, the flow pattern classification of the bores was reported by Yeh and Ghazali [3] and Yeh et al. [4], dividing into strong and weak bores. A strong bore (or fully developed bore) refers to the condition $h_1/h_0 > 2.0$ (where h_1 and h_0 are the upstream and downstream still water depths), while a weak bore (or undular bore) to $h_1/h_0 < 2.0$, along with the leading wave breaking for $1.6 < h_1/h_0 < 2.0$. On the other hand, Shimozono [5] reported a classification slightly different from that of Yeh and Ghazali [3] and Yeh et al. [4] with a strong, transitional and weak bore if $h_1/h_0 > 2.0$, $1.75 < h_1/h_0 < 2.0$ and $h_1/h_0 \leq 1.75$, respectively.

Comprehensive studies were undertaken to look into variations in the free surface profiles/elevations of undular bores accompanied by leading waves propagating over horizontal bottom with constant water depth. Analytical investigations included Peregrine [6], Soares Frazao and Zech [7], Gavrilyuk et al. [8], and Kharif and Abid [9] as well as numerical ones comprised by Madsen and Svendsen [10] and Gavrilyuk et al. [8]. Experimental works (Favre [11]; Treske [12]; Stansby et al. [13]) examined spatio-temporal variation in the free surface profiles of undular bores.

Parallelly, theoretical and numerical models were developed to study the free surface variations, propagation speeds of bore front, velocity fields and swash zone dynamics for bores traveling over sloping beaches. The 1st-order non-linear long wave theory (Ho and Meyer [14]; Shen and Meyer [15,16]), finite difference method (Packwood [17]), numerical solutions of shallow-water equation (Guard and Baldock [18]) were also reported. The 2D Reynolds Averaged Navier–Stokes (RANS) solver coupled with k-ε turbulence closure and a volume of fluid method (Zhang and Liu [19]) as well as a new model (closed-form non-linear evolution equation) derived from the Euler equation (Kharif and Abid [9]) were subsequently presented.

Experimental studies also illustrated the maximum run-up height (Miller [20]; Yeh [21]), bed shear stress on swash zone (Barnes et al. [22]), and velocity profiles measured by Particle Image Velocimetry (PIV) (O'Donoghue et al. [23]; Kikkert et al. [24]). In the above studies, the leading waves riding on a pure bore were observed but not elucidated. More recently, the pioneering work on the relationship between the free surface elevation and velocity field of the leading waves was presented in Lin et al. [2] using a high-speed PIV (HSPIV). However, the effect of the leading waves on acceleration and pressure gradient of undular bore was not addressed.

As reported by Jensen et al. [25], accelerations are more difficult to obtain by PIV/HSPIV than velocities due to fast spatio-temporal variation in the flow field of solitary waves traveling on a steep

beach. To our best knowledge, only two numerical works (Puleo et al. [26]; Higuera et al. [27]) and several PIV/HSPIV or pressure-transducer measurement results (Chang and Liu [28]; Jensen et al. [25,29]; Pedrozo-Acuna et al. [30]; Lin et al. [31]) have been reported for the solitary/periodic waves. However, no study was undertaken to investigate the characteristics of acceleration and pressure gradient of the bore propagating over a sloping beach. In the present study, the temporal variations of (local, convective, and total) accelerations as well as pressure gradient of the generated undular bore propagating over a 1:20 sloping beach are elucidated in a specified section.

The experimental set-ups and instrumentations are introduced in the next section. Some results and discussions associated with the free surface elevations and velocity fields/profiles are presented in Section 3. The calculation method of accelerations and pressure gradient are detailed in Section 4 with some tables illustrating the calculation process. The temporal variations of accelerations and pressure gradient are then presented in Section 5. Finally, concluding remarks are given in Section 6.

2. Experimental Set-Ups and Instrumentations

A flume of length 13.0 m, width 0.25 m, and depth 0.5 m was used to perform the bore experiments. A vertical gate, made of steel plate and placed 375.9 cm from the upstream flume end, was opened instantly with the help of a servo-motor mounted on a steel frame structure (see Figure 1a,b). The toe of the 1:20 sloping beach model (made of acrylic sheet) was positioned 270.5 cm downstream from the gate. Before opening the gate, the upstream and downstream water depths correspond to h_1 and h_0. The sudden opening of the gate thus forms the so-called dambreak-generated bore with the water depth ratio h_1/h_0.

A Cartesian coordinate system, (x, y), is used with its origin $(0, 0)$ located at the toe of the sloping beach. Positive x is oriented in the horizontal shoreward direction and the positive y in the vertical upward direction over the beach surface (Figure 1c). The corresponding velocity components of the generated bore (gb) are represented by $([u]_{gb}, [v]_{gb})$. Further, a translated ordinate, y' $(=y - x/20)$, is also used to mark the height above the beach surface. Herein, t' is time, with $t' = 0$ s denoting the instant for the gate being open initially at $x = -270.5$ cm. Further, t is time, with $t = 0$ s identifying the moment when the crest of the 1st leading wave is right at the section where the toe of the sloping beach is located (i.e., $x = 0$).

The free surface elevations were measured using four capacitance-type wave gauges. The 1st, 2nd, and 3rd wave gauges were placed at $x = -150.0$, 0, and 101.7 cm, respectively. Note that the still-water-shoreline (SWS) formed by the intersection of the still-water surface and the sloping beach is located at $x = x_{sws} = 180.0$ cm. The 4th wave gauge was installed at the specified measuring section (SMS) at $x = x_{SMS} = 194.0$ cm, where the bed was dry prior to arrival of the bore front.

A HSPIV system, with a framing rate ≥ 1000 Hz, was used to measure the 2D instantaneous velocity fields while the bore traveling on the sloping beach. The system comprised an argon-ion laser, a cylindrical lens, and a high-speed digital camera. The 5 Watt argon-ion laser head (Innova-300, Coherent Inc., Santa Clara, CA, USA) was employed as the light source. Titanium dioxide (TiO2) particles having a refractive index of 2.6 and a mean diameter of 1.8 μm were used as seeding particles. The cylindrical lens was employed to convert the laser beam into a fan-shaped light sheet of about 1.5 mm in thickness. Then the light sheet was diverted upwards via flume glass bottom to illuminate the seeding particles on a vertical plane (which is 10.0 cm from the flume glass sidewall on the camera side). The camera (Phantom M310, Vision Research Inc., Wayne, NJ, USA), with a maximum framing rate of 3260 Hz under the largest resolution of 1280×800 pixels, was used to capture the instantaneous particle-laden images. A field of view (FOV), 14.0 cm wide and 8.75 cm high with a resolution of 0.01094 cm/pixel, was centered on the SMS. For calculation of accelerations and pressure gradient of the bore front and leading waves, the camera framing rate was set at 1000 Hz. The sampling interval between two neighboring images is thus $\Delta t_{framing} = 1.0 \times 10^{-3}$ s. The HSPIV algorithm allows one instantaneous velocity field to be determined from a pair of images, starting at the 64×64 pixel interrogation window-size and ending at the 8×8 pixel.
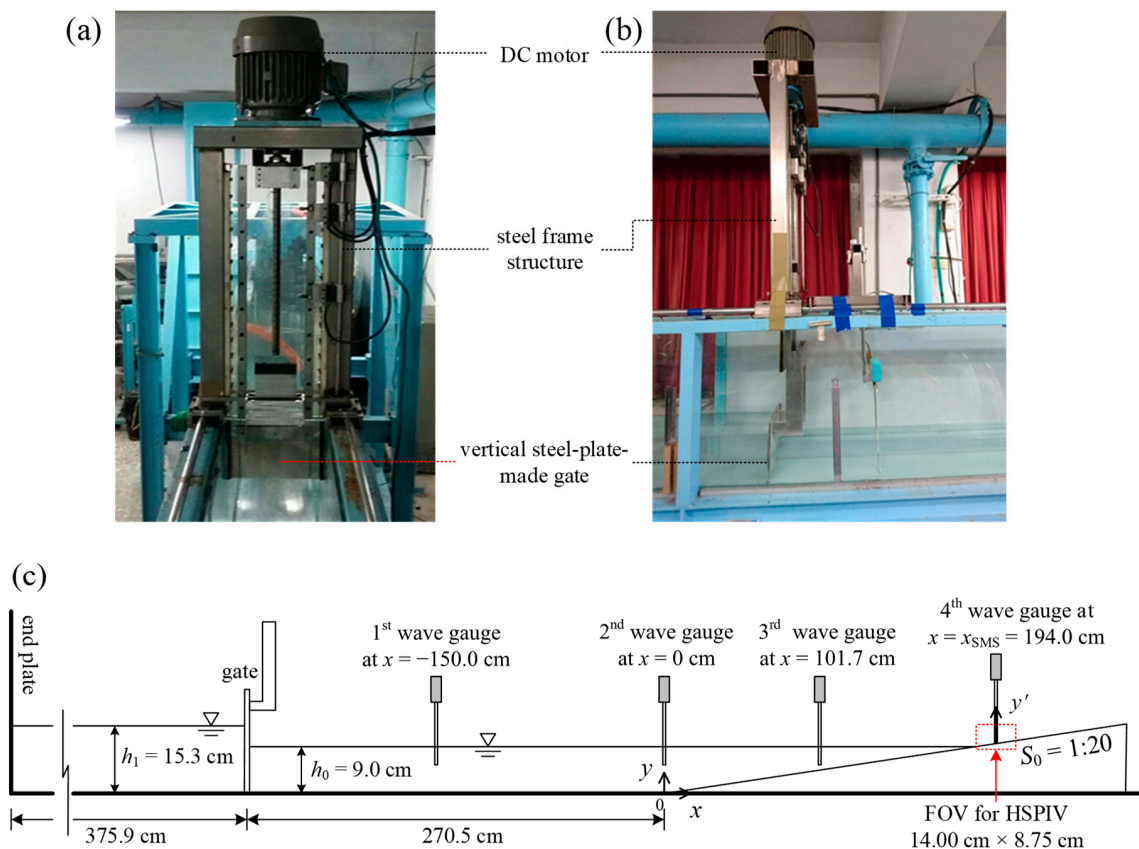
Figure 1. Photos showing the gate with its supporting steel frame structure mounted on the flume, (**a**) front view; (**b**) side view; (**c**) schematic diagram showing sloping beach model and coordinate system, together with installation of four wave gauges at $x = -150.0$, 0, 101.7, and 194.0 cm as well as deployment of field of view (FOV) for high-speed Particle Image Velocimetry (HSPIV) measurements.

According to Yeh and Ghazali [3], Yeh et al. [4], and Shimozono [5], an undular (or weak) bore occurs downstream of the suddenly lifted gate for $h_1/h_0 \leq 1.75$. For higher value of h_1/h_0, the flow field induced by the generated bore is more towards transitional state with a certain degree of irregularity. On the other hand, for lower value of h_1/h_0, the free surface produced downstream of the gate is apt to be a nearly streamlined profile without occurrence of the leading waves (Soares Frazao and Zech [7], and Kharif and Abid [9]). To highlight the role played by the leading waves on modifying the velocity fields/profiles of the pure (undular) bore, the experimental condition with $h_1/h_0 = 1.70$ ($h_1 = 15.3$ cm and $h_0 = 9.0$ cm) was eventually selected as the target experiment. Simultaneous measurements of the velocity field and free surface profile/elevation were repeated for 30 runs in the vicinity of the SMS. An ensemble-averaged method followed by a subsequent moving average technique was used to smoothen the velocity fields/profiles and free surface elevations.

3. Preliminary Tests

At first, a repeatability test for the free surface profile and internal flow structure of the generated bore right downstream of the gate for -268.5 cm $\leq x \leq -243.5$ cm was performed using the camera at a framing rate of 200 Hz. Figure 2a–d shows four images with the internal flow fields underlying the instantaneous free surface profiles, which were randomly selected from 20 repeated runs at the same instants $t' = 0.21$ s (or $t = -2.464$ s). For easily viewing the flow structure, the range of the images is confined only between $x = -268.5$ cm and $x = -258.5$ cm. Due to the influence of the initial horizontal and vertical accelerations of water mass beneath the gate, a jet-like flow issues from the upstream side to the shallower quiescent water mass on the downstream side of the gate.
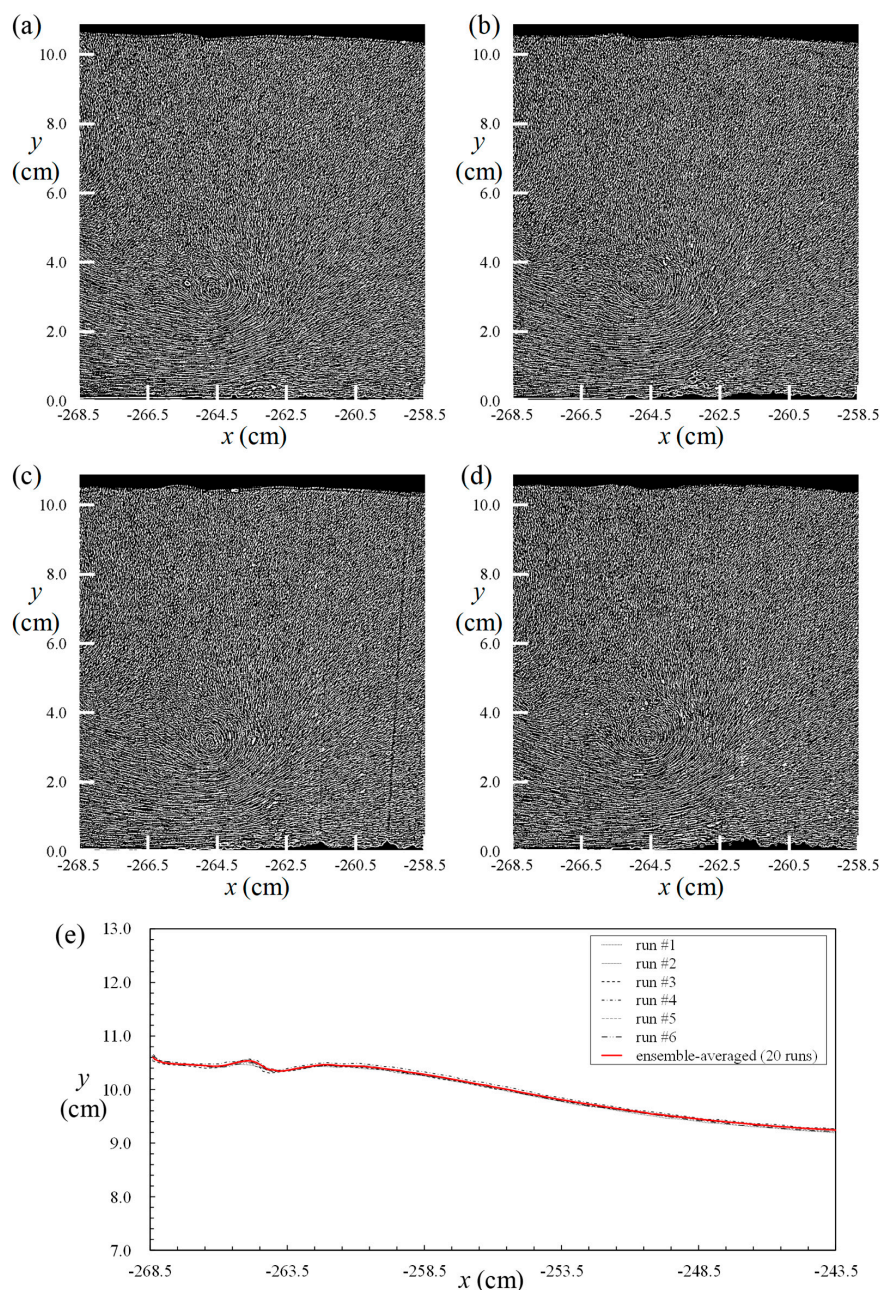
Figure 2. (**a–d**) Images taken at $t' = 0.21$ s (or $t = -2.464$ s) soon after opening gate for four different repeated runs, show instantaneous flow fields underlying free surface profile right downstream of gate; (**e**) comparison of instantaneous free surface profiles among six different repeated runs and ensemble-averaged result for 20 runs.

This results in formation of the shear layer and associated vortex structures right downstream of the gate. It is surprisingly found that the flow patterns and core positions of the vortex structures are very similar. This fact highlights lack of prominently irregular fluctuations and high repeatability of the internal flow structure induced by the generated bores for different runs. In addition, the free surface profiles illustrated in the four images, which are summarized in Figure 2e (with those of two additional runs), are almost identical to the ensemble-averaged results of 20 runs. The (relative) value of the global standard deviation for a specified run, which deviates most from the ensemble-averaged result of 20 runs, is only as small as 0.033 cm (0.37% with respect to the downstream still-water depth

h_0 = 9.0 cm). All the free-surface evidences also demonstrate high repeatability of the free surface profile of the generated bore right downstream of the gate.

Secondly, a repeatability test for the free surface elevation of the generated bore $[\eta(t)]_{gb}$ was conducted for 30 repeated runs at $x = 0$ using a capacitance-type wave gauge. Note that $[\eta(t)]_{gb}$ is measured with reference to h_0. As seen in Figure 3a, for clarity and easy comparison, only the results of six runs, randomly selected from the repeated 30 runs, are plotted along with the ensemble-averaged counterpart of 20 runs (which is, in fact, almost same as that of 30 runs due to convergence of the data trend). The generated bore is comprised of a pure bore accompanied by a series of leading waves. It is surprisingly found that any one of the results for six individual runs is almost identical to those of the other five runs. Namely, good agreement is evidenced not only at the crest and trough levels of the leading waves but also at any level of the pure bore without leading wave. The results of six individual runs are also almost same as that of the ensemble-averaged counterpart, only with small differences. The maximum value of the global standard deviation for the specified run, which at most biases the ensemble-averaged result of 30 repeated runs, is 0.041 cm, equivalent to a relative value of 0.8% with reference to the crest level (5.11 cm) of the 1st leading wave at $t = 0$ s. It is pertinent to mention that the identical trend for the associated results of the free surface elevation obtained at $x = 194.0$ cm was reported in Lin et al. [2] (Figure 2d on page 79 of reference [2]). Based on the fact abovementioned, the free surface profile/elevation of the generated bore is identified to be produced repeatedly with high repeatability in the present study.
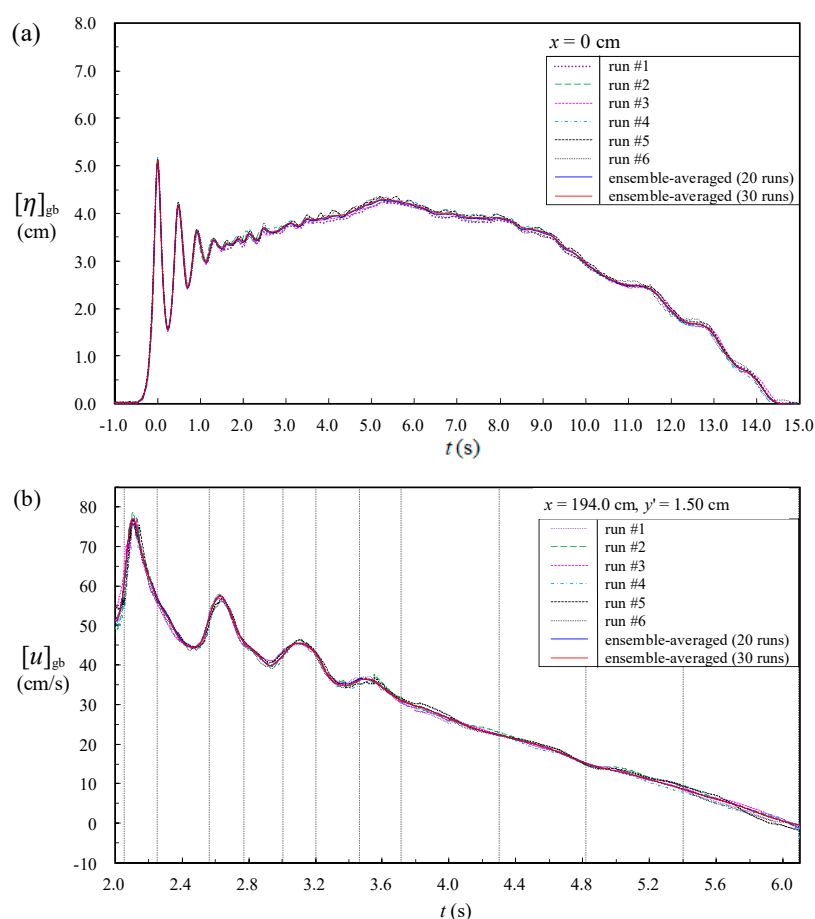

Figure 3. (a) Comparison of free surface elevations among six different repeated runs and ensemble-averaged result for 30 repeated runs at $x = 0$; (b) comparison of time series of horizontal velocity among six distinct runs and ensemble-averaged result for 30 repeated runs at $x = 194.0$ cm and $y' = 1.50$ cm.

Thirdly, Figure 3b presents the time series of the horizontal velocity of the generated bore $[u(t)]_{gb}$ for six individual runs, together with the counterpart of the ensemble-averaged result for 30 repeated runs, measured at the SMS with $(x, y') = (194.0, 1.50)$ cm. A very similar trend between any two time series and fairly good accordance with the ensemble-averaged result for each of the tested runs are evidenced. The relative value of the global standard deviation is 1.70% with respect to the maximum horizontal velocity (77.01 cm/s) occurring at $t = 2.106$ s for the crest phase of the 2nd leading wave (due to breaking of the 1st leading wave at $x = 101.7$ cm, to be stated later). This fact strongly justifies high repeatability of the horizontal velocity of the generated bore propagating on the sloping beach.

4. Free Surface Elevation and Velocity Field/Profile of Bore

4.1. Free Surface Elevations over Horizontal Bottom and Sloping Beach

Figure 4 shows a series of temporal variation in the (ensemble-averaged) free surface elevation of the generated bore, $[\eta(t)]_{gb}$ and $[\eta'(t)]_{gb}$, at $x = 0$, 101.7 and 194.0 cm, respectively. Note that the still-water surface intersects the slope at $x_{SWS} = 180.0$ cm and $[\eta'(t)]_{gb}$ is gauged upwards from the beach surface.
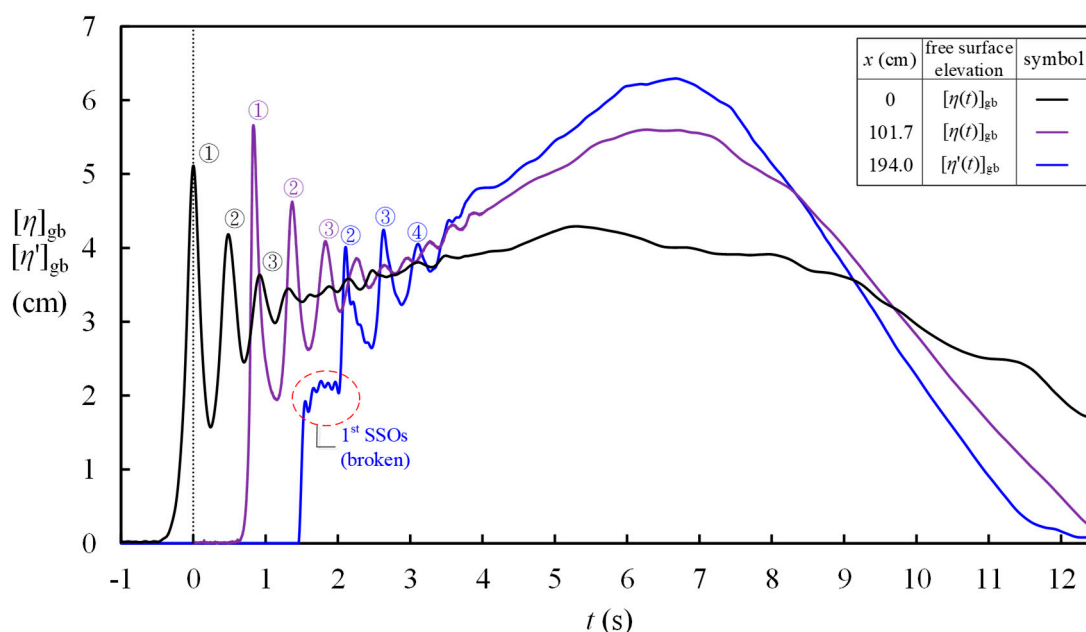

Figure 4. Time series of free surface elevations measured at three different sections between $x = 0$ cm and $x = x_{SMS} = 194.0$ cm (i.e., specified measuring section (SMS)). Note that crests of nth leading wave measured at distinct x are marked by circled n in different colors.

For $x = 0$ and 101.7 cm in Figure 4, at least four prominent leading waves propagate shoreward by the bore with its front reaching $x = 0$ and 101.7 cm at $t = 0$ and 0.836 s, respectively. These waves experience the shoaling process during the early run-up stage of generated bore, resulting in an increase in wave height and change in wave period (or frequency), thus confirming the dispersive feature of the leading waves (Lin et al. [2]; Soares Frazao and Zech [7]; Kharif and Abid [9]; Tissier et al. [32]; Bjorkavag and Kalisch [33]). The leading waves eventually break at different positions for distinct times, along with the generated bore reaching the maximum run-up height of 8.86 cm at $t = 5.195$ s (see Figure 5). The 1st leading wave breaks at the breaking point (bp1) $x = x_{bp1} = 101.7$ cm for $t = 0.836$ s with an air-entrained plunging breaker. For $t > 0.836$ s and $x > 101.7$ cm, the bore front is followed by a bubbly turbulent flow, thus leading to energy dissipation of the 1st leading wave. Under such a situation, rise in the free surface elevation of the 1st leading wave no longer exists. Instead, a plateau-shaped free surface with some small-scale oscillations (SSOs) in the time series of $[\eta'(t)]_{gb}$ is

observable after passing of the bore front and prior to arrival of the 2nd leading wave for 1.550 s < t < 2.055 s (see Figure 4 for the SMS at x_{SMS} = 194.0 cm).
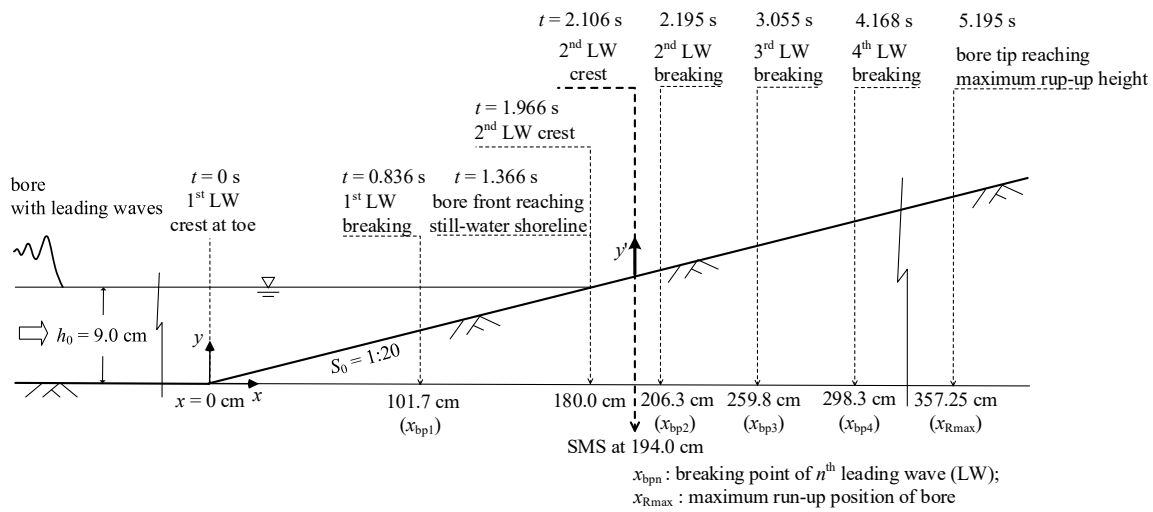

Figure 5. Spatial variation of breaking point x_{bpn} for nth leading wave (with n = 1–4).

4.2. Velocity Fields/Profiles during Run-Up Motion for 2.0 s ≤ t ≤ 3.462 s at SMS

Figure 6a–c presents three (ensemble-averaged) instantaneous velocity fields of the generated bore for 191.0 cm ≤ x ≤ 197.0 cm (extracted from the FOV), corresponding to the crest of the 2nd leading wave before, right and after passing the SMS at t = 2.093, 2.106 and 2.119 s, respectively. The time interval between these two neighboring figures is Δt = 0.013 s (=13 × Δ$t_{framing}$ = 13/1000 s). Relatively uniform velocity profiles extending upward to the free surface are clearly evidenced for different instants and at distinct sections. Such a uniform horizontal velocity in the external stream of the generated bore is defined as $[u_u(x, t)]_{gb}$, determined from the partially depth-averaged value of the horizontal velocities inside the relatively uniform zone (i.e., excluding the velocity gradient zone in the boundary layer flow or internal stream). The maximum value of $[u_u(x, t)]_{gb}$ of the generated bore takes place under the crest of the 2nd leading wave, say $([(u_u)]_{gb})_{max}$ = 79.9 cm/s at x = 192.0 cm, $([(u_u)]_{gb})_{max}$ = 81.7 cm/s at x = x_{SMS} = 194.0 cm, and $([(u_u)]_{gb})_{max}$ = 82.9 cm/s at x = 196.2 cm for Figure 6a–c, respectively. The data trend demonstrates that the generated bore at the SMS is accelerated and decelerated temporally as well as spatially decelerated and accelerated shoreward for t = 2.093 and 2.119 s. Such a feature is attributable to the effect of pre-/post-passing of the 2nd leading wave crest through the SMS.
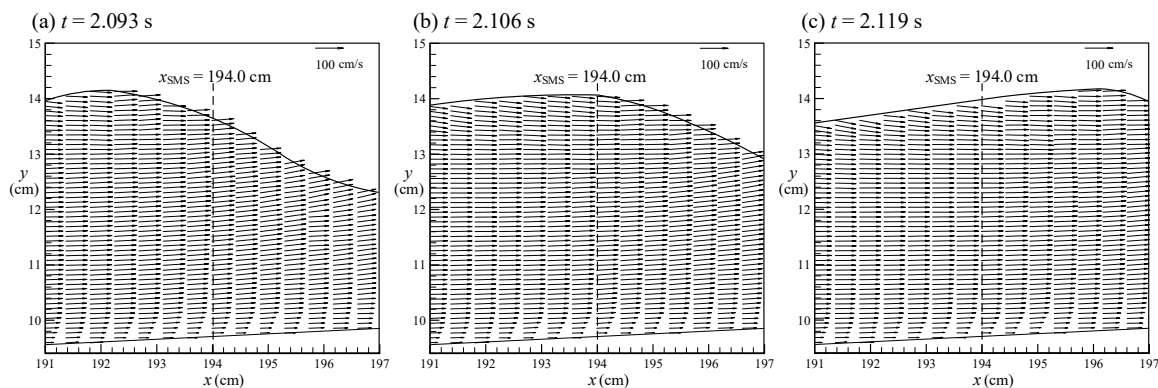

Figure 6. Ensemble-averaged velocity fields at (**a**) t = 2.093 s; (**b**) t = 2.106 s; (**c**) t = 2.119 s during run-up motion of generated bore.

Figure 7a shows the time series of ensemble-averaged data for the combined free surface elevation of the generated bore, $\eta'(t)$, measured at the SMS for 30 repeated runs. As addressed in Appendix A,

the frequency contents in free surface elevation of the leading waves, ranging between 2.00 and 4.20 Hz, are higher than those of the pure bore (from 0.067 to 0.10 Hz) around the SMS. Therefore, using fast Fourier transform (FFT) and inverse fast Fourier transform (IFFT) with a frequency demarcation f_{fd} = 0.707 Hz (see Figure A1a,b in Appendix A for the details), the free surface elevation mainly contributed from the 2nd to 5th leading waves, $[\eta'(t)]_{lw}$, is shown in Figure 7b for the frequency contents greater than f_{fd}. Meanwhile, the free surface elevation provided by the pure bore, $[\eta'(t)]_{pb}$ $(=[\eta'(t)]_{gb} - [\eta'(t)]_{lw})$, is obtained for the frequency contents less than f_{fd} = 0.707 Hz, as illustrated in Figure 7a (as marked by dashed line). Given that the 1st leading wave has broken at x = 101.7 cm for t = 0.836 s before reaching the still-water shoreline at x_{SWS} = 180.0 cm (see Figure 5). The remaining four correspond to the 2nd, 3rd, 4th, and 5th leading waves. The instants identified in the time histories of the bore and leading waves by employing distinct vertical lines (each has a circled number) are all tabulated in the sub-table of Figure 7a,b.
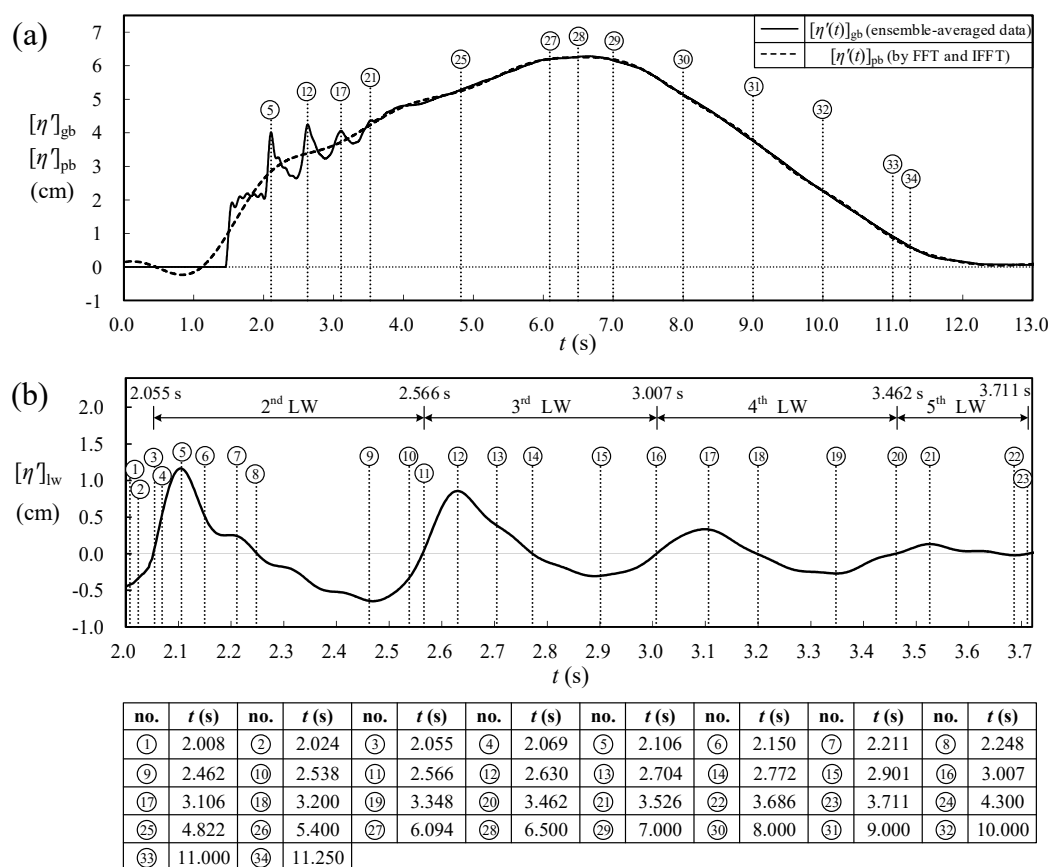

no.	t (s)	no.	t (s)	no.	t (s)	no.	t (s)	no.	t (s)	no.	t (s)	no.	t (s)	no.	t (s)
①	2.008	②	2.024	③	2.055	④	2.069	⑤	2.106	⑥	2.150	⑦	2.211	⑧	2.248
⑨	2.462	⑩	2.538	⑪	2.566	⑫	2.630	⑬	2.704	⑭	2.772	⑮	2.901	⑯	3.007
⑰	3.106	⑱	3.200	⑲	3.348	⑳	3.462	㉑	3.526	㉒	3.686	㉓	3.711	㉔	4.300
㉕	4.822	㉖	5.400	㉗	6.094	㉘	6.500	㉙	7.000	㉚	8.000	㉛	9.000	㉜	10.000
㉝	11.000	㉞	11.250												

Figure 7. Time series of ensemble-averaged data for free surface elevations of (**a**) generated bore $[\eta'(t)]_{gb}$ and pure bore $[\eta'(t)]_{pb}$ measured at SMS; (**b**) *n*th leading waves $[\eta'(t)]_{lw}$ (with *n* = 2–5).

In Figure 7a,b for 2.000 s ≤ t ≤ 2.055 s, the temporal variation of $[\eta'(t)]_{lw}$ just reflects the free surface rise from the local trough level of the final SSOs in the broken 1st leading wave at t = 2.008 s (the circled 1), via the ascending stage at t = 2.024 s (the circled 2), then to the ending/zero-up-crossing phase of the 1st/2nd leading wave at t = 2.055 s (the circled 3). The uniform horizontal velocities of the generated bore at these three phases are equal to $[u_u]_{gb}$ = 50.4, 53.4, and 59.5 cm/s (see the circled 1–3 in Figure 7a,b and Figure 8). The trend points out the increase in $[u_u(t)]_{gb}$ with increasing free surface elevation from the trough phase. In addition, a very prominent increase of $[u_u(t)]_{gb}$ appears for 2.055 s ≤ t ≤ 2.106 s with $[u_u]_{gb}$ = 59.5 cm/s at t = 2.055 s, $[u_u]_{gb}$ = 66.7 cm/s for the ascending level at t = 2.069 s, and $[u_u]_{gb}$ = 81.7 cm/s for the crest level of the 2nd leading wave at t = 2.106 s (see the

circled 3–5 in Figure 7a,b and Figure 8). This indicates that the generated bore is accelerated temporally in the onshore direction during the first rising stage of the 2nd leading wave for 2.055 s ≤ t ≤ 2.106 s.
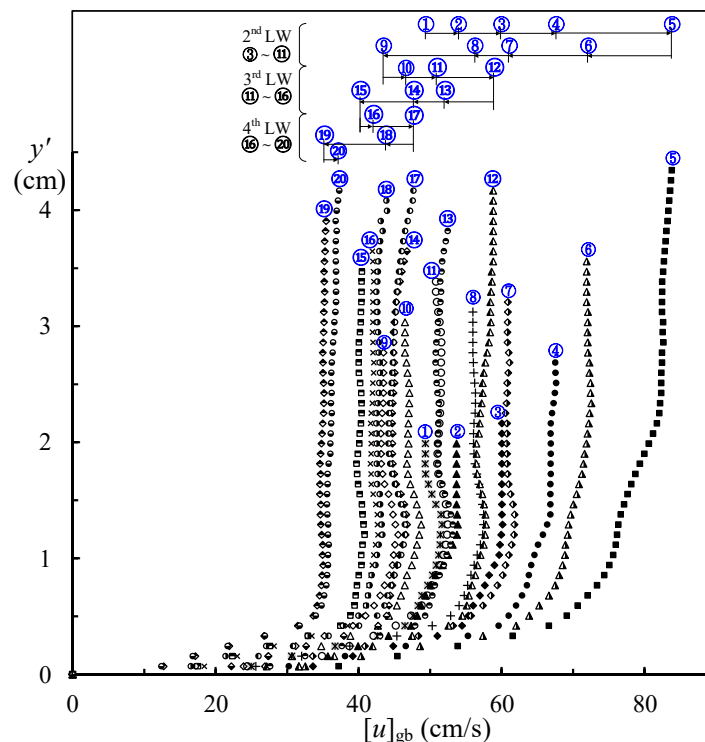

Figure 8. Temporal variation of horizontal velocity profile of generated bore with 2nd, 3rd, and 4th leading waves obtained at SMS for 2.008 s ≤ t ≤ 3.462 s during run-up motion. Corresponding times labeled from circled 1 to 20 are listed in sub-table of Figure 7b.

For 2.106 s ≤ t ≤ 2.462 s in Figure 7a,b, the free surface elevation changes from the crest level to the two descending levels at t = 2.150 and 2.211 s with $[u_u]_{gb}$ = 78.1 and 61.1 cm/s (see the circled 5–7 in Figure 7a,b and Figure 8). Next, it steps over the zero-down-crossing level at t = 2.248 s with $[u_u]_{gb}$ = 56.5 cm/s and then goes further down to the trough level of the 2nd leading wave with $[u_u]_{gb}$ = 43.9 cm/s at t = 2.462 s (the circled 7–9). This trend shows that $[u_u(t)]_{gb}$ keeps decreasing with time for 2.106 s ≤ t ≤ 2.462 s, implying that the generated bore is temporally decelerated shoreward within this time interval.

Furthermore, for 2.462 s ≤ t ≤ 2.566 s in Figure 7a,b, the free surface elevation varies from the trough level, via the ascending level at t = 2.538 s with $[u_u]_{gb}$ = 47.3 cm/s (see the circled 10 in Figure 7a,b and Figure 8), to the ending/zero-up-crossing level of the 2nd/3rd leading wave at t = 2.566 s with $[u_u]_{gb}$ = 51.5 cm/s (the circled 11). Note that the temporal variations in $[u_u(t)]_{gb}$ of the 3rd and 4th leading waves are similar to that of the 2nd leading wave, as evidenced in the serial changes for 2.566 s ≤ t ≤ 3.007 s (the circled 11–16) and 3.007 s ≤ t ≤ 3.462 s (the circled 16–20).

The features of temporal variation in the uniform horizontal velocity of generated bore, $[u_u(t)]_{gb}$, during passing of the nth leading wave (with n = 2–4) through the SMS are summarized as (1) successive increase from a certain positive value up to a maximum positive value as the free surface elevation changes from the zero-up-crossing to crest level (see the circled 3–5, 11–12, and 16–17 on the top of Figure 8). (2) Decreasing continuously from a maximum positive value at the crest level, via a certain positive value at the zero-down-crossing level, then down to a positive minimum one at the trough level (see the circled 5–9, 12–15 and 17–19). (3) Consecutive increase from a positive minimum at the trough level to a relatively larger value at the ending level (see the circled 9–11, 15–16, and 19–20). This fact indicates the effect of velocity shift on increasing/decreasing $[u_u(t)]_{gb}$ due to continuous ascending/descending of the free surface of the nth leading wave. The first rising/descending free

surface of the *n*th leading wave (with *n* = 2–4) just corresponds to pre-/post-passing of its wave crest. For easy comprehension, variation trend of the acceleration or deceleration in the uniform horizontal velocity of the generated bore is summarized schematically in Figure 9 with respect to the phases of the leading waves (with *n* = 2–4).
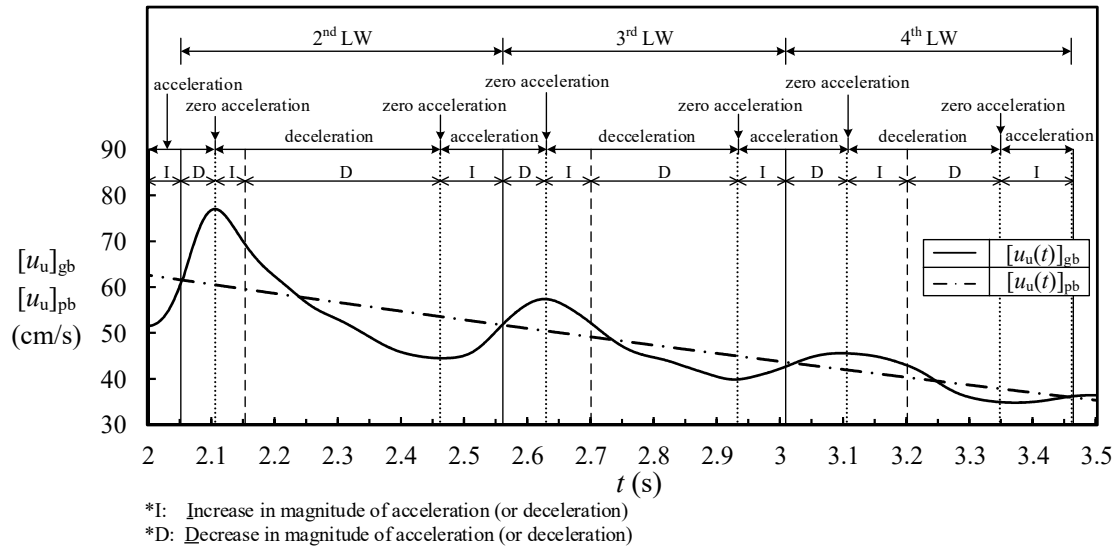

*I: Increase in magnitude of acceleration (or deceleration)
*D: Decrease in magnitude of acceleration (or deceleration)

Figure 9. Schematic diagram of variation in acceleration or deceleration in uniform horizontal velocity of the generated bore.

For *t* ≥ 3.462 s, the influence of the *k*th leading waves (with *k* ≥ 5) on the velocity distribution becomes less significant as compared with those from the 2nd to 4th. As supporting evidence, Figure 10 shows two velocity fields at *t* = 3.462 and 3.526 s (marked by black and red arrows) for 191.0 cm ≤ *x* ≤ 197.0 cm. The velocity fields are nearly identical both in the magnitudes and directions. These correspond to the zero-up-crossing and crest phases of the 5th leading wave, at which the uniform horizontal velocities of the generated bore are in order equal to $[u_u]_{gb}$ = 36.3 and 36.5 cm/s. The uniform horizontal velocities of the pure bore at *t* = 3.462 and 3.526 s amount to $[u_u]_{pb}$ = 35.9 and 34.9 cm/s (addressed later in Equation (1)). This implies that the horizontal velocities contributed by the 5th leading wave at *t* = 3.462 and 3.526 s are equal to $[u_u]_{lw}$ = 0.4 and 1.6 cm/s. Therefore, the relative deviation of the maximum shift of the horizontal velocity influenced by the 5th leading wave is equal to 4.4% with respect to $[u_u]_{gb}$ = 36.5 cm/s. Similarly, the relative deviations for the 6th and 7th leading waves are 2.7% and 1.4% (not shown), respectively. The data trend confirms that the free surface variation of the *k*th leading wave (with *k* ≥ 5) has a decreasing effect on the velocity shift of generated bore. Consequently, their effect on the velocity distribution during the run-up is thus ignored. In the following, the magnitudes of the horizontal velocity in the profiles at SMS for 3.462 s ≤ *t* ≤ 6.094 s are considered as being contributed mostly by the pure bore.

Figure 11 illustrates the temporal variation of the horizontal velocity profile of the generated bore for 3.462 s ≤ *t* ≤ 6.094 s (also see the circled 20–27 in Figure 7a). As mentioned above, the magnitudes of the velocities in the two profiles at *t* = 3.462 and 3.526 s (the circled 20 and 21) are nearly the same due to the combined effect of the increasing velocities by passing of the 5th leading-wave crest and the temporally decreasing velocities of the pure bore. An analogous situation is also observed for *t* = 3.686 and 3.711 s (the circled 22 and 23). However, larger onshore velocities are observed at *t* = 3.686 s (i.e., corresponding to the trough level of the 5th leading wave) than those at *t* = 3.711 s (i.e., the ending/zero-up-crossing phase of the 5th/6th leading wave). This is because the major decrease in the horizontal velocity of the pure bore accompanied by the minor increase in the horizontal velocity of the 5th leading wave during the second rising stage for 3.686 s ≤ *t* ≤ 3.711 s. Afterwards, the uniform horizontal velocity of the generated (or pure) bore decreases continuously from $[u_u]_{gb} \approx [u_u]_{pb}$ =

23.0 cm/s at $t = 4.30$ s (the circled 24) to $[u_u]_{gb} = [u_u]_{pb} = 0$ at $t = 6.094$ s (the circled 27). Note that flow reversal takes place close to the beach surface for $t > 4.822$ s and the velocity profile at $t = 6.094$ s is characterized by the uniform horizontal velocity exactly equal to zero in the middle portion. Moreover, occurrence of the shoreward stream near the free surface and the offshore stream of flow reversal close to the beach surface is clearly evidenced.
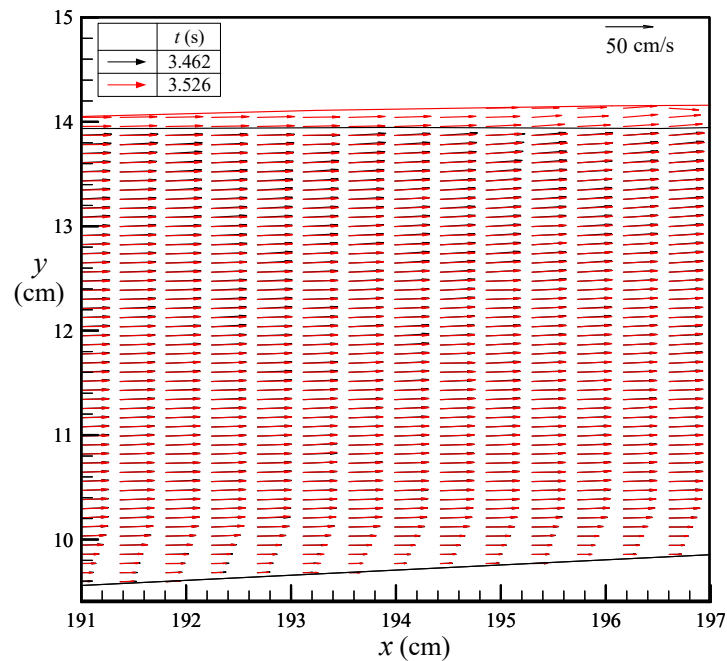

Figure 10. Velocity fields for 191.0 cm $\leq x \leq$ 197.0 cm at $t = 3.462$ and 3.526 s (marked by black and red arrows), corresponding to zero-up-crossing and crest phases of 5th leading wave during run-up motion of generated bore.
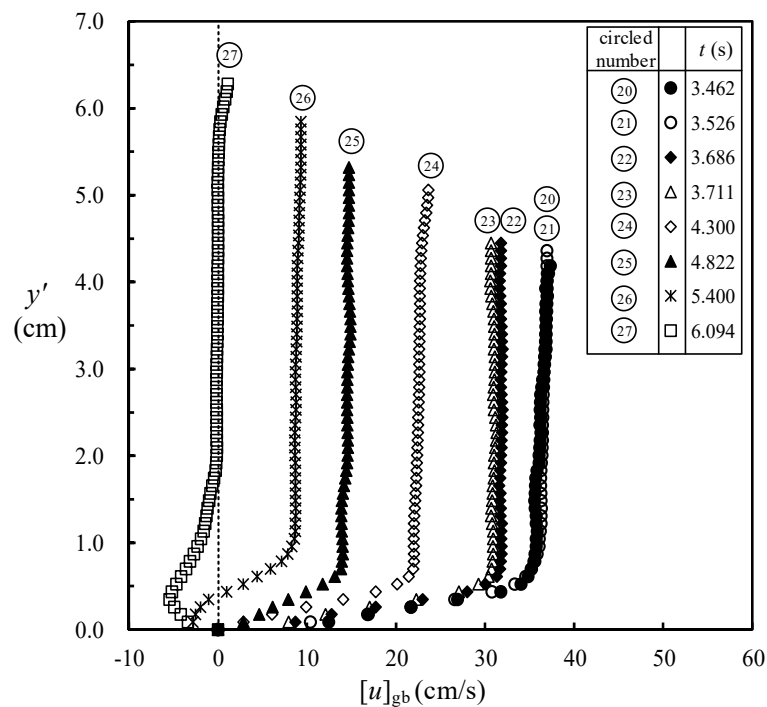

Figure 11. Temporal variation of horizontal velocity profile of generated bore obtained at SMS for 3.462 s $\leq t \leq$ 6.094 s during run-up motion (as labeled from circled 20 to 27 in Figure 7a,b).

4.3. Velocity Fields/Profiles during Run-Down Motion for 6.094 s ≤ t < 12.00 at SMS

Figure 12 presents temporal variation of the horizontal velocity profile of pure bore at the SMS for 6.094 s ≤ t < 12.00 s. The phases of the velocity profiles correspond to those of the free surface elevation shown in Figure 7a,b (see the circled 27–34). The uniform horizontal velocities $[u_u(t)]_{pb}$ are all found to take negative values and increase successively in their magnitudes with increasing time t. For example, $[u_u(t)]_{pb}$ = 0, −21.6, −44.4, −62.5, and −63.6 cm/s at t = 6.094, 8.00, 10.00, 11.35, and 11.75 s, respectively. The data trend highlights the positive/negative "local acceleration" of the external stream of the pure bore in the offshore/onshore direction during the run-down at the SMS.
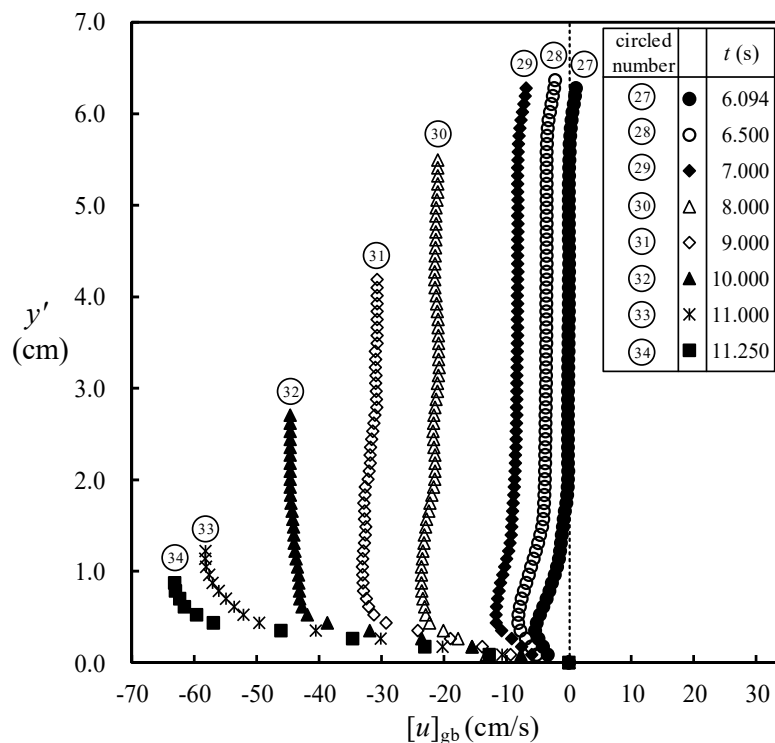
circled number		t (s)
㉗	●	6.094
㉘	○	6.500
㉙	◆	7.000
㉚	△	8.000
㉛	◇	9.000
㉜	▲	10.000
㉝	✳	11.000
㉞	■	11.250

Figure 12. Temporal variation of horizontal velocity profile of pure bore obtained at SMS for 6.094 s ≤ t ≤ 11.250 s during run-down motion (as labeled from circled 27 to 34 in Figure 7a,b).

In summary, the temporal variations in the free surface elevation and horizontal velocity profile of pure bore with acceleration or deceleration feature throughout the full water depth are shown in Figure 13. The effect of velocity shift is neglected at all of the phases marked by the red solid points (which are located at or very close to the zero-up-crossings of the leading waves). Therefore, the magnitudes of the onshore/offshore uniform horizontal velocities in the profiles of pure bore are justified to decrease/increase continuously for 2.000 s ≤ t ≤ 6.094 s/6.094 s ≤ t < 12.00 s during run-up/run-down motion. The result also exhibits that the pure bore is decelerated/accelerated temporally in the onshore/offshore direction for both intervals. It is pertinent to indicate the difference in the acceleration or deceleration feature between the pure bore and the leading waves, as shown clearly in Figures 9 and 13, respectively.
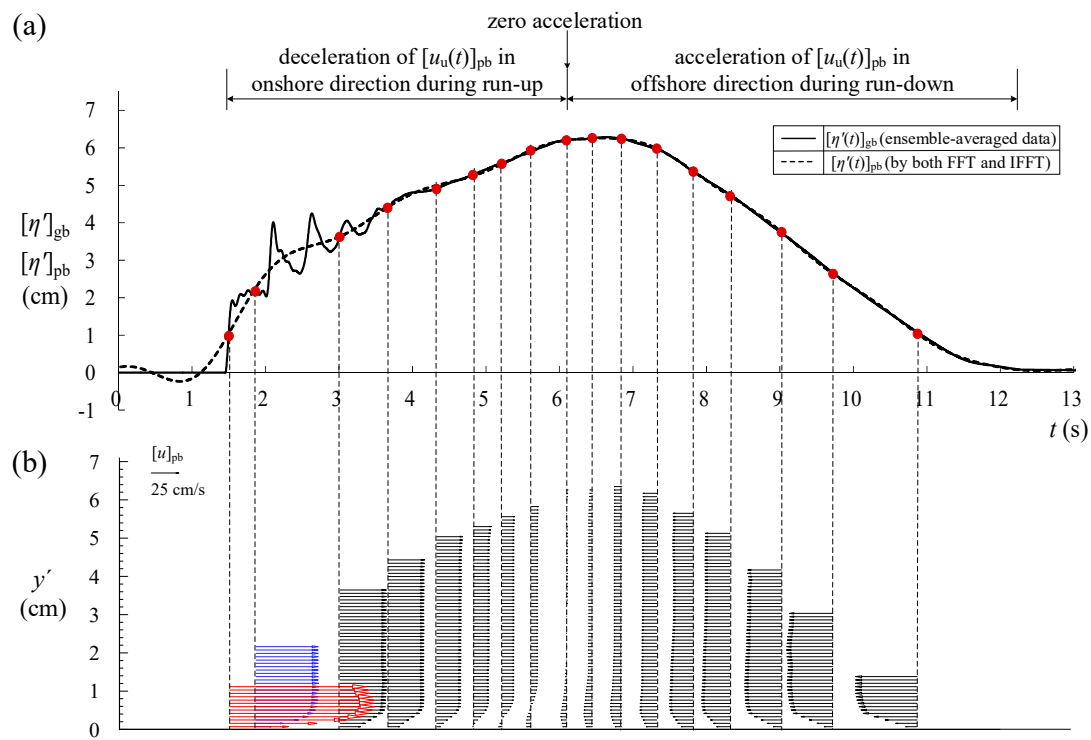
Figure 13. Temporal variations of (**a**) $[\eta'(t)]_{gb}$ and $[\eta'(t)]_{pb}$; (**b**) horizontal velocity profiles of pure bore throughout instantaneous water depths during run-up and run-down at SMS.

4.4. Uniform Horizontal Velocity of Pure Bore at SMS for 2.00 s ≤ t < 12.00 s

The temporal variation in the free surface elevation of the leading waves $[\eta'(t)]_{lw}$ ($=[\eta'(t)]_{gb} - [\eta'(t)]_{pb}$) is shown again in Figure 14a. Two pairs of the time histories of the horizontal velocities of the generated and pure bores, $[u(t)]_{gb}$ and $[u(t)]_{pb}$, for $y' = 1.50$ and 2.00 cm at the SMS, are presented in Figure 14b. The time series of horizontal velocity of the "pure bore" at $y' = 1.50$ cm are almost identical to those obtained at $y' = 2.00$ cm. This fact still holds true for the remaining heights away from the boundary layer, clearly indicating the horizontal velocity profile of pure bore is fairly uniform (except that within the boundary layer). At around the zero-up-crossing and zero-down-crossing levels of the free surface elevation of the nth leading wave (with $n = 2$–4), the horizontal velocity contributed only by the leading waves is equal or close to 0. This fact allows the horizontal velocity, obtained at a specified height and contributed only by the pure bore, to be estimated at the SMS.

Based on the data points located on or close to the dashed line shown in Figure 14b, the onshore uniform horizontal velocity of the pure bore, $[u_u(t)]_{pb}$, during the run-up is estimated by the exponential decay function (Lin et al. [2]; O'Donoghue et al. [23]; Kikkert et al. [24]):

$$[u_u(t)]_{pb} = 152.379 \times \exp[-0.143(t - 1.460)] - 78.416 \qquad \text{for } 2.00 \text{ s} \le t \le 6.094 \text{ s}, \qquad (1)$$

namely, for the run-up motion of pure bore, Equation (1) confirms the temporally successive decrease in the onshore uniform horizontal velocity and continuous shoreward deceleration (i.e., with the negative "local acceleration"). Nevertheless, the pure bore while ridden by the leading waves is decelerated/accelerated spatially and accelerated/decelerated temporally in the onshore direction during the ascending/descending free surface of the nth leading wave (with $n = 2$–4). The result demonstrates again the effect of pre-/post-passing of the leading wave crest on the velocity distribution of the generated bore.

During run-down for 6.094 s ≤ t < 12.00 s, the generated bore, behaving as a pure bore without the leading waves, moves offshore at the SMS. The time histories of free surface elevation and horizontal velocity profile of the pure bore, $[\eta'(t)]_{pb}$ ($=[\eta'(t)]_{gb}$) and $[u_u(t)]_{pb}$ ($=[u_u(t)]_{gb}$), are illustrated

in Figure 14a,b. Further, the temporal variation of the offshore uniform horizontal velocity during run-down is illustrated in Figure 15 with its trend expressed by a regressed linear equation:

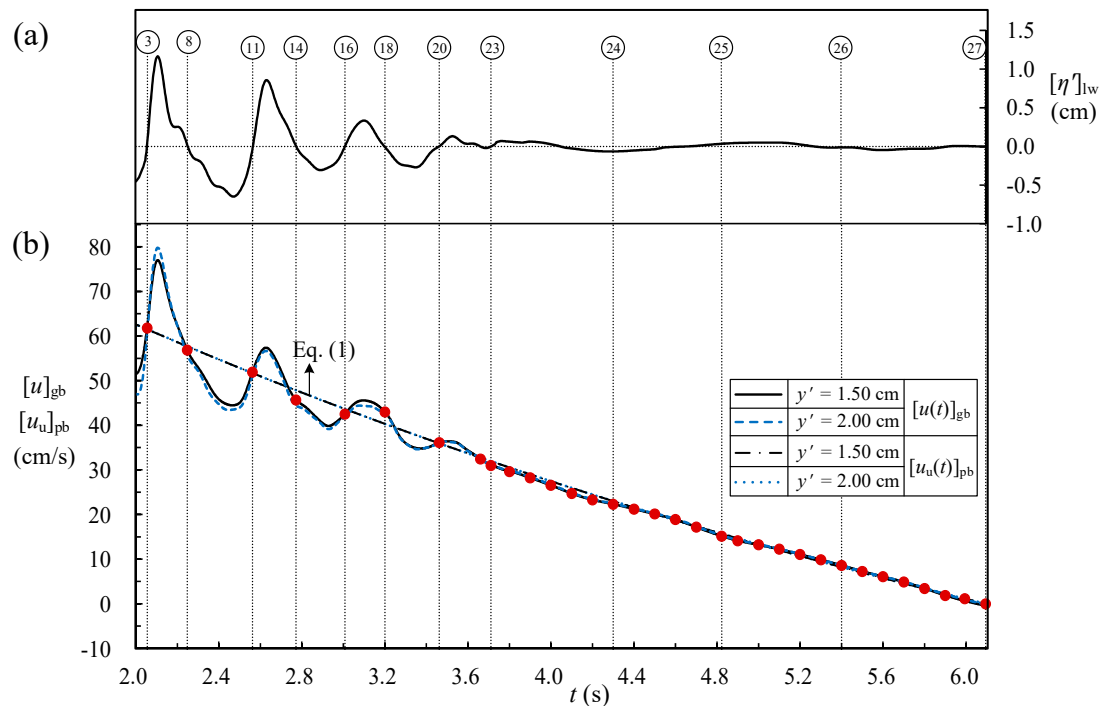$$[u_u(t)]_{pb} = -11.242t + 68.508 \qquad \text{for } 6.094 \text{ s} \leq t < 12.00 \text{ s.} \tag{2}$$

Figure 14. Time series of (**a**) $[\eta'(t)]_{lw}$; (**b**) $[u(t)]_{gb}$ and $[u_u(t)]_{pb}$ for $y' = 1.50$ and 2.00 cm at SMS for $2.000 \text{ s} \leq t \leq 6.094 \text{ s}$. Velocities $[u_u(t)]_{pb}$ at both y' are almost identical and overlap together as shown in (**b**). Times varying from circled 3 to 27 are presented in sub-table of Figure 7a,b.
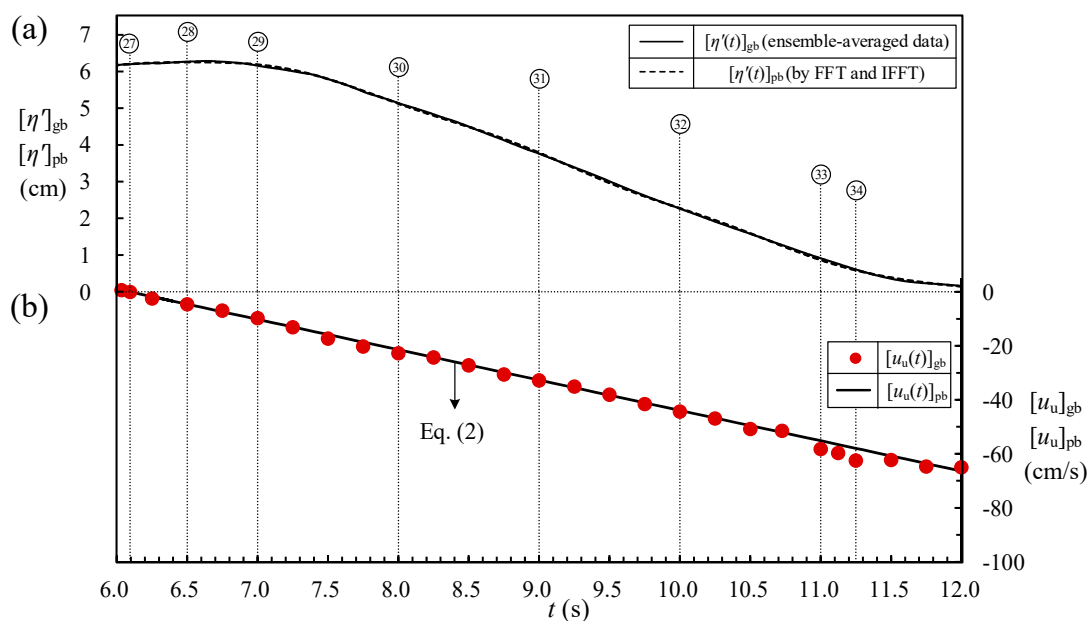

Figure 15. Temporal variations of (**a**) $[\eta'(t)]_{gb}$ and $[\eta'(t)]_{pb}$; (**b**) $[u_u(t)]_{gb}$ and $[u_u(t)]_{pb}$ obtained at SMS for $6.094 \text{ s} \leq t < 12.000 \text{ s}$. Note that times changing from circled 27 to 34 are shown in sub-table of Figure 7a,b.

The linear increase in the magnitude of the offshore uniform horizontal velocity with increasing t is highlighted in Equation (2). The fact indicates the acceleration/deceleration of the external stream of the pure bore in the offshore/onshore direction during the run-down.

5. Calculation Method for Accelerations and Pressure Gradient in Horizontal Direction

5.1. Definitions Based on Navier–Stokes Equation

Computation of accelerations and pressure gradient of the external stream of the generated bore in the x direction is based on the horizontal component of the Navier–Stokes equation (with the positive value shoreward):

$$[\partial u/\partial t + u\partial u/\partial x + v\partial u/\partial y]_{gb} = [-(1/\rho)\partial p/\partial x - g\partial h_p/\partial x + \mu/\rho(\partial(\partial u/\partial x)/\partial x + \partial(\partial u/\partial y)/\partial y)]_{gb}, \quad (3)$$

with ρ = the density of water, μ = the dynamic viscosity of water, and h_p = the gravitational force potential. The gravity term in Equation (3) is equal to 0. With long wave and neglecting the boundary layer effect, $[\partial(\partial u/\partial x)/\partial x]_{gb}$ and $[\partial(\partial u/\partial y)/\partial y]_{gb}$ should be fairly small (to be further stated later). Therefore, Equation (3) is rewritten as:

$$\begin{aligned}[\partial u/\partial t + u\partial u/\partial x + v\partial u/\partial y]_{gb} &= [A_1(x, y, t) + A_c(x, y, t)]_{gb} = [A_t(x, y, t)]_{gb} \\ &= -(1/\rho)[\partial p(x, y, t)/\partial x]_{gb} = -[P(x, y, t)]_{gb},\end{aligned} \quad (4)$$

where $[A_1(x, y, t)]_{gb}$ $(=[\partial u(x, y, t)/\partial t]_{gb})$, $[A_c(x, y, t)]_{gb}$ $(=[A_{c1}(x, y, t) + A_{c2}(x, y, t)]_{gb}$ with $[A_{c1}(x, y, t)]_{gb}$ $= [u(x, y, t) \times \partial u(x, y, t)/\partial x]_{gb}$ and $[A_{c2}(x, y, t)]_{gb} = [v(x, y, t) \times \partial u(x, y, t)/\partial y]_{gb})$, and $[A_t(x, y, t)]_{gb}$ are the local, convective, and total accelerations in the horizontal direction, respectively. From Equation (4), the pressure gradient $[P(x, y, t)]_{gb}$ $(=(1/\rho)[\partial p(x, y, t)/\partial x]_{gb} = -[A_1(x, y, t) + A_c(x, y, t)]_{gb} = -[A_t(x, y, t)]_{gb})$ is obtained accordingly.

It is pertinent to mention that the HSPIV sampling frequency is 1000 Hz, resulting in a time lapse of $\Delta t_{framing} = 1.0 \times 10^{-3}$ s between any two consecutive images. The tests are carried out by trial-and-error, employing distinct time intervals Δt and spatial intervals Δx to calculate the local and 1st convective accelerations of the external stream of the generated bore, $[A_1(x, y, t)]_{gb}$ and $[A_{c1}(x, y, t)]_{gb}$. However, for computing the 2nd convective acceleration $[A_{c2}(x, y, t)]_{gb}$, only one spatial interval in the y direction is used with $\Delta y = 0.0873$ cm. Obtaining reasonable accelerations is more difficult than velocities because of fast spatio-temporal fluctuations even in the fine PIV/HSPIV measurements (Jensen et al. [25]). To find out representative results, the partially depth-averaged method (with the velocities obtained outside/inside the boundary layer are included/excluded) is used to calculate the local and 1st convective accelerations. The influences of distinct time and spatial intervals on the partially depth-averaged (pda) values of both $\{[A_1(x, y, t)]_{gb}\}_{pda}$ and $\{[A_{c1}(x, y, t)]_{gb}\}_{pda}$ are evaluated as below.

For a given measuring section (e.g., at the SMS), the relationship among the partially depth-averaged values of the local acceleration $\{[A_1(t)]_{gb}\}_{pda}$, the 1st and 2nd convective accelerations $\{[A_{c1}(t)]_{gb}\}_{pda}$ and $\{[A_{c2}(t)]_{gb}\}_{pda}$, the total acceleration $\{[A_t(t)]_{gb}\}_{pda}$ as well as the pressure gradient $\{[P(t)]_{gb}\}_{pda}$ of the external stream of the generated bore in the horizontal direction can be expressed as:

$$\begin{aligned}&\{[\partial u(t)/\partial t]_{gb}\}_{pda} + \{[u(t) \times \partial u(t)/\partial x]_{gb}\}_{pda} + \{[v(t) \times \partial u(t)/\partial y]_{gb}\}_{pda} \\ &= \{[A_1(t)]_{gb}\}_{pda} + \{[A_{c1}(t)]_{gb}\}_{pda} + \{[A_{c2}(t)]_{gb}\}_{pda} \\ &= \{[A_1(t)]_{gb}\}_{pda} + \{[A_c(t)]_{gb}\}_{pda} \\ &= \{[A_t(t)]_{gb}\}_{pda} \\ &= -\{[(1/\rho)\partial p(t)/\partial x]_{gb}\}_{pda} \\ &= -\{[P(t)]_{gb}\}_{pda}\end{aligned} \quad (5)$$

5.2. Calculation Example for Local Acceleration

In the following calculations, five Δt intervals are tested by trial-and-error using the central difference scheme to ensure the reasonable values of the local accelerations. Due to rapid ascending or descending of the free surface, the forward or backward difference scheme is used for calculation near the free surface.

The values of y' ($=y - x/20$) as well as the data sets for three horizontal velocity profiles of the generated bore $[u(y')]_{gb}$, obtained at the SMS ($x = x_{SMS} = 194.0$ cm) for $t = 2.059$, 2.069, and 2.079 s (i.e., with $\Delta t = 0.010$ s), are tabulated in order from the leftmost side of Table A1 in Appendix B. The velocity profiles, $[u(y')]_{gb}$ and $[v(y')]_{gb}$, for $t = 2.069$ s at $x = 193.04$ and 194.96 cm as well as for $t = 2.059$, 2.069 and 2.079 s at the SMS are shown in Figure 16a,c as well as Figure 16b, respectively. For $\Delta t = 0.010$ s, the calculated values of the local acceleration of generated bore, $[A_1(y')]_{gb}$, at different heights y' are shown in the 7th column of Table A1, revealing that the magnitudes range from 387.4 to 661.2 cm/s^2 with drastic vertical variations. The partially depth-averaged value of the local acceleration, $\{[A_1(t)]_{gb}\}_{pda}$, shown at the bottom of the 7th column in Table A1 amounts to 530.3 cm/s^2.
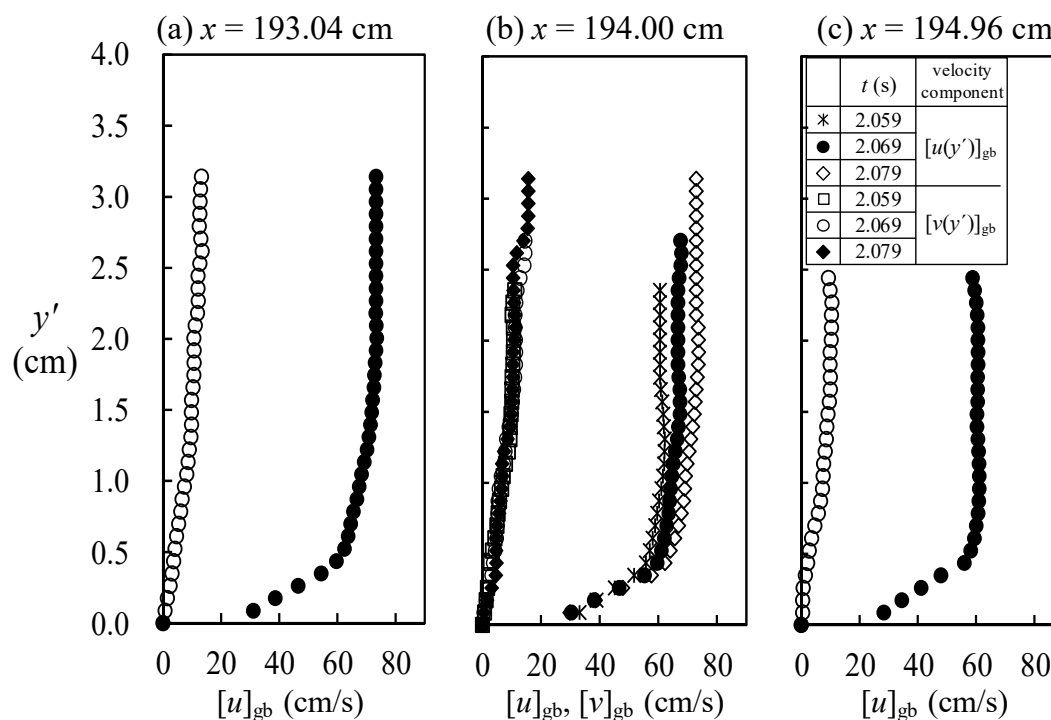

Figure 16. Velocity profiles, $[u(y')]_{gb}$ and $[v(y')]_{gb}$, obtained for (**a**,**c**) $t = 2.069$ s at $x = 193.04$ and 194.96 cm; (**b**) $t = 2.059$, 2.069, and 2.079 s at SMS.

Four more intervals of $\Delta t = 0.005$, 0.008, 0.012, and 0.015 s are tested additionally for evaluating their influences on the values of $[A_1(y')]_{gb}$ at the SMS. The velocity profiles are not shown here for brevity. The computed values of $[A_1(y'')]_{gb}$ for the time intervals vary considerably not only in the vertical direction for a specified Δt, but also at the identical height for different Δt (see the 5th, 6th, 8th, and 9th columns in Table A1). To find out the representative values, the partially depth-averaged values of the local acceleration, $\{[A_1]_{gb}\}_{pda}$, are thus calculated. For $\Delta t = 0.005$, 0.008, 0.010, 0.012, and 0.015 s, the values of $\{[A_1]_{gb}\}_{pda}$ are 588.8, 525.1, 530.0, 503.6, and 477.4 cm/s^2 (with a conditional average of 519.6 cm/s^2 for the middle three, see the bottom of Table A1 and Figure A2a). The results reveal that the values of $\{[A_1]_{gb}\}_{pda}$ of the middle three do not differ so much, and that the relative deviations, D_r, of $\{[A_1]_{gb}\}_{pda}$ with reference to the conditional average vary from 1.1% to 3.1%. However, for relatively smaller/greater time interval, say $\Delta t = 0.005$ and 0.015 s, the relative deviations D_r equal to 13.3% and 8.1% (see the bottom in the 5th–9th columns of Table A1 and Figure A2a) become large.

The examination testifies the appropriateness of using adequate time intervals to reasonably obtain $\{[A_1(t)]_{gb}\}_{pda}$ close to 519.6 cm/s^2 at $t = 2.069$ s if the criterion for the relative deviation being less than 4% is adopted.

It is worth noting that, at the beginning of the calculation for the acceleration, a convergence test for the calculated results of $\{[A_1(t)]_{gb}\}_{pda}$ at different time intervals Δt was performed but with failure in obtaining the convergent value of $\{[A_1(t)]_{gb}\}_{pda}$. Namely, it is nearly impossible to obtain the optimal Δt that corresponds to a convergent value of $\{[A_1(t)]_{gb}\}_{pda}$. This is why the influences of different time intervals on accelerations should be evaluated by trial-and-error. The aim is to find a promising range of the time intervals, within which the relative deviation of each calculation result of $\{[A_1(t)]_{gb}\}_{pda}$ would only vary within 4.0% of the conditional average. Similarly, it is also impossible to obtain the optimal Δx that corresponds to a convergent value of $\{[A_{c1}(t)]_{gb}\}_{pda}$ in the next subsection. For easy understanding, a flow chart that illustrates the calculation procedure to determine a promising value of either $\{[A_1(t)]_{gb}\}_{pda}$ or $\{[A_{c1}(t)]_{gb}\}_{pda}$ is presented in Figure 17.
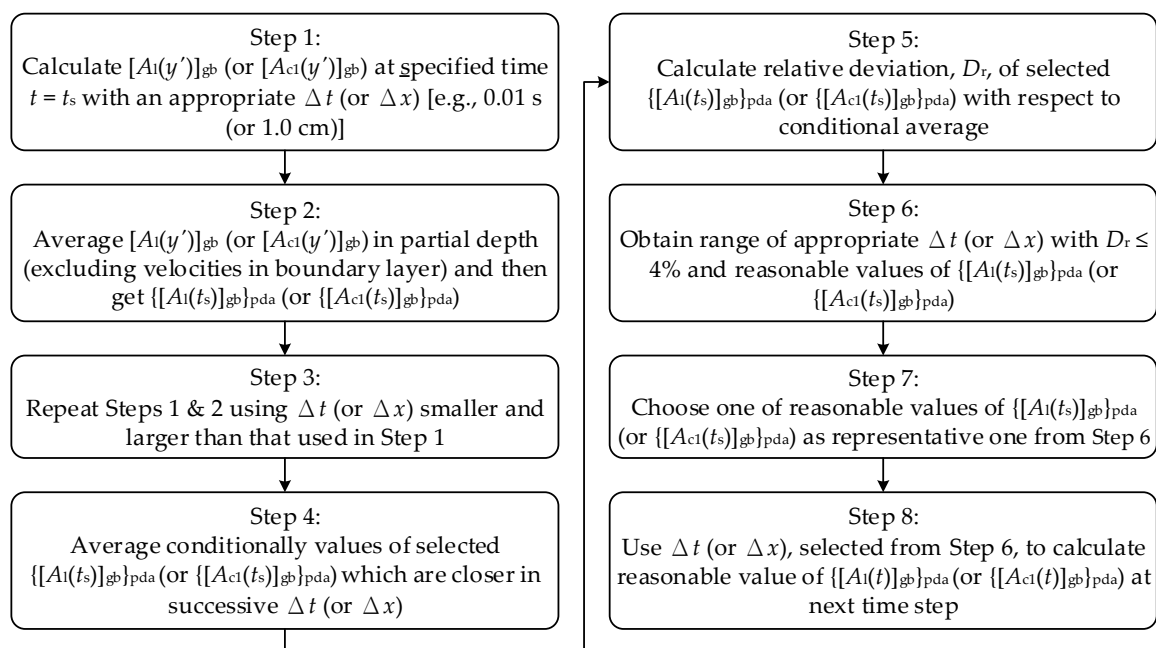

Figure 17. Flow chart showing calculation process to determine promising value of $\{[A_1(t)]_{gb}\}_{pda}$ or $\{[A_{c1}(t)]_{gb}\}_{pda}$.

5.3. Calculation Example for 1st Convective Acceleration at SMS

As seen in Table A2 of Appendix B, the values of y' as well as three horizontal velocity distributions $[u(y')]_{gb}$ measured at $x = 193.04$, 194.0, and 194.96 cm (i.e., with $\Delta x = 0.96$ cm) for $t = 2.069$ s are tabulated from the 1st to 4th columns, respectively. For calculating $[A_{c1}(y')]_{gb}$ at the SMS, six spatial intervals Δx equal to 0.26, 0.52, 0.70, 0.96, 1.49, and 2.00 cm are subsequently tested. The computed values of $[A_{c1}(y')]_{gb}$ do vary drastically in the vertical direction for a specified Δx or even at the same height for distinct Δx (from the 5th to 10th columns). The partially depth-averaged values of the 1st convective acceleration, $\{[A_{c1}]_{gb}\}_{pda}$, are equal to −258.6, −359.5, −384.3, −378.2, −284.3, and −259.5 cm/s^2 (see the bottom of Table A2 from the 5th to 10th columns and Figure A2b). The average computed from the 2nd to 4th values amounts to −374.0 cm/s^2 and their relative deviations are 3.9%, 2.8%, and 1.1%, respectively, all less than 4%. The small relative deviations indicate promising selection of the three spatial intervals (i.e., $\Delta x = 0.52$, 0.70, and 0.96 cm) to compute reasonable values of $\{[A_{c1}]_{gb}\}_{pda}$ toward the conditional average of −374.0 cm/s^2 for $t = 2.069$ s. Nevertheless, the relative deviations for the 1st, 5th, and 6th values stated above are equal to 30.9%, 24.0%, and 30.6%, demonstrating that too

smaller/larger spacing interval does result in significant bias (also see the bottom of Table A2 from the 5th to 10th columns and Figure A2b).

5.4. Calculation Example for 2nd Convective and Total Accelerations and Pressure Gradient at SMS

Similar to the previous calculation example, the values of heights y' with $\Delta y = 0.0873$ cm and velocity data, $[v(y')]_{gb}$ and $[u(y')]_{gb}$, at the SMS are listed for $t = 2.069$ s from the 1st to 4th columns of Table A3 in Appendix B. Table A3 also shows the values of the 2nd convective and total accelerations, $[A_{c2}(y')]_{gb}$ and $[A_t(y')]_{gb}$, as well as the values of the pressure gradient, $[P(y')]_{gb}$, of the external stream at the SMS. The values of $[A_{c2}(y')]_{gb}$ and $[A_t(y')]_{gb}$ computed at distinct locations vary prominently both in the vertical direction and even at the same height. The partially depth-averaged values of the accelerations and pressure gradient equal to $\{[A_{c2}]_{gb}\}_{pda} = 16.6$ cm/s^2, $\{[A_t]_{gb}\}_{pda} = 168.4$ cm/s^2, and $\{[P]_{gb}\}_{pda} = -168.4$ cm/s^2 are listed at the bottom of Table A3. Note that $\{[P]_{gb}\}_{pda} = -168.4$ cm/s^2 reveals that the external stream of the generated bore at $t = 2.069$ s is subject to the favorable pressure gradient in the onshore direction.

Distinct Δt and Δx intervals are further tested for different times at the SMS to obtain the promising values of $\{[A_1]_{gb}\}_{pda}$, $\{[A_{c1}]_{gb}\}_{pda}$, $\{[A_{c2}]_{gb}\}_{pda}$, $\{[A_t]_{gb}\}_{pda}$, and $\{[P]_{gb}\}_{pda}$ which would not have prominent changes due to small variation of the time and spatial intervals. It is found that use of $\Delta t = 0.008, 0.010,$ and 0.012 s as well as $\Delta x = 0.96$ cm can acquire reasonable values of accelerations with all relative deviations less than 4.0% with respect to the conditional averages. Further, an examination of the term $\{[(\mu/\rho)\partial(\partial u/\partial x)/\partial x + \partial(\partial u/\partial y)/\partial y]_{gb}\}_{pda}$ exhibits the magnitudes of only $O(10^{-1})$ cm/s^2, demonstrating its contribution is so small such that its effect can be ignored.

6. Results and Discussions

In this section, the results of accelerations and pressure gradient are generalized in the dimensionless form. Herein, the downstream still-water depth h_0 and linear wave celerity C_0 ($=(gh_0)^{1/2}$) are used as the representative length and velocity scales, respectively, together with $(h_0/g)^{1/2}$ and g being the representative time and acceleration scales. All of the dimensionless variables are shown with an asterisk superscript. Accordingly, (x^*, y^*) are the non-dimensional horizontal and vertical coordinates, along with $([u^*]_{gb}, [v^*]_{gb})$ and $([u^*]_{pb}, [v^*]_{pb})$ being the non-dimensional velocity components. A translated ordinate, $y'^* (=y^* - x^*/20)$, is used to represent the non-dimensional height above the beach surface. η'^* is the non-dimensional free surface elevation. $[A_1^*]_{gb}$, $[A_{c1}^*]_{gb}$, $[A_{c2}^*]_{gb}$, $[A_c^*]_{gb}$, $[A_t^*]_{gb}$, and $[P^*]_{gb}$ are the non-dimensional local acceleration, 1st term of convective acceleration, 2nd term of convective acceleration, (total) convective acceleration, total accelerations, and pressure gradient of the generated bore, respectively. Further, $[A_1^*]_{pb}$, $[A_{c1}^*]_{pb}$, $[A_{c2}^*]_{pb}$, $[A_c^*]_{pb}$, $[A_t^*]_{pb}$, and $[P^*]_{pb}$ are the non-dimensional counterparts of the pure bore. The partially depth-averaged values of the non-dimensional pressure gradients of both generated bore and pure bore are then represented by $\{[P^*]_{gb}\}_{pda}$ and $[P^*]_{pb}$, respectively.

6.1. Local Acceleration of Pure Bore at SMS

As stated in Section 4.4, the onshore/offshore uniform horizontal velocity of the pure bore at the SMS can be predicted by Equation (1)/(2). The uniform horizontal velocity is originally defined as the partially depth-averaged value of the horizontal velocities ranging within the fairly uniform zone (i.e., excluding the velocities inside the boundary layer flow or internal stream). Accordingly, the non-dimensional uniform horizontal velocity of pure bore $[u_u^*(t^*)]_{pb}$ at the SMS can be described by two following equations:

$$[u_u^*(t^*)]_{pb} = 1.6217 \times \exp[-0.0137(t^* - 15.243)] - 0.8345 \quad \text{for } 20.881 \le t^* \le 63.623, \tag{6}$$

$$[u_u^*(t^*)]_{pb} = -0.0115t^* + 0.7317 \quad \text{for } 63.623 \le t^* < 125.284. \tag{7}$$

The non-dimensional local acceleration of the external stream of the pure bore, $[A_1^*(t^*)]_{pb}$ $(=\partial[u_u^*(t^*)]_{pb}/\partial t^*)$, during the run-up and run-down can be estimated as follows:

$$[A_1^*(t^*)]_{pb} = -0.0222 \times \exp[-0.0137(t^* - 15.243)] \quad \text{for } 20.881 \leq t^* \leq 63.623, \tag{8}$$

$$[A_1^*(t^*)]_{pb} = -0.0115 \quad \text{for } 63.623 \leq t^* < 125.284. \tag{9}$$

The value of $[A_1^*(t^*)]_{pb}$ should be equal to $\{[A_1^*(t^*)]_{pb}\}_{pda}$ because of the uniform feature in the external stream of the pure bore.

Based on Equations (8) and (9), Figure 18 shows variation of $\{[A_1^*(t^*)]_{pb}\}_{pda}$ with t^* for the external stream of the pure bore during the run-up and run-down for $20.881 \leq t^* \leq 63.623$ and $63.623 \leq t^* < 125.284$, respectively. It can be observed that onshore deceleration of pure bore with a temporally exponential decay trend takes place during the run-up for $20.881 \leq t^* \leq 63.623$. For example, $\{[A_1^*]_{pb}\}_{pda}$ $= [A_1^*]_{pb} = -0.0206, -0.0167, -0.0138$, and -0.0115 at $t^* = 20.881, 36.144, 50.343$, and 63.623, respectively. On the other hand, the non-dimensional acceleration with a constant of 0.0115 in the offshore direction occurs during the run-down for $63.623 \leq t^* < 125.284$, demonstrating an increase in the offshore uniform horizontal velocity with time.
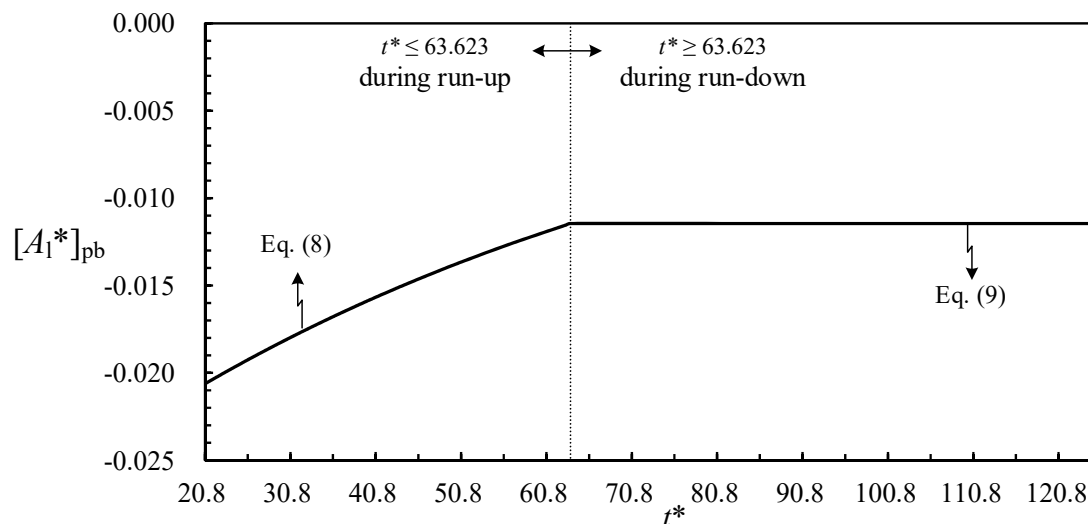

Figure 18. Relationship of non-dimensional local acceleration $[A_1^*(t^*)]_{pb}$ versus non-dimensional time t^* for pure bore during run-up and run-down motions for $20.881 \leq t^* \leq 63.623$ and $63.623 \leq t^* < 125.284$, respectively.

6.2. Local Acceleration of Generated Bore at SMS

Figure 19a,b presents the relationships of $[\eta'^*(t^*)]_{lw}$, $[u^*(t^*)]_{gb}$, and $[u^*(t^*)]_{pb}$ versus t^* for $y'^* = 0.1667$ at the SMS. Figure 19c illustrates the variations of $\{[A_1^*(t^*)]_{gb}\}_{pda}$, $\{[A_c^*(t^*)]_{gb}\}_{pda}$, and $\{P^*_{gb}\}_{pda}$ of the external stream, all obtained also at the SMS. Due to breaking of the 1st leading wave at $x^* > 11.30$ for $t^* > 8.728$, the most evident rise in the free surface elevation of the 1st leading wave does not exist. Instead, a plateau-shaped free surface with some SSOs in the time series of $[\eta'^*(t^*)]_{gb}$ is seen before arrival of the 2nd leading wave at the SMS for $t^* \geq 21.455$ (see Figures 4 and 7a). The influences of the 2nd to 5th leading waves on the values of $\{[A_1^*(t^*)]_{gb}\}_{pda}$ are discussed in the following subsections.

6.2.1. Influence of 2nd Leading Wave

As seen in Figure 19c, $\{[A_1^*(t^*)]_{gb}\}_{pda}$ increases drastically from 0.0061 and 0.0489 at $t^* = 20.881$ and 20.964 (i.e., near the final trough level of the SSOs of the broken 1st leading wave). Further, $\{[A_1^*(t^*)]_{gb}\}_{pda}$ reaches 0.1147 and 0.3839, respectively, at $t^* = 21.131$ and 21.455 (i.e., the zero-up-crossing

phase of the 2nd leading wave, circled 3) and then soon arrives at the positive maximum of 0.5403 at $t^* = 21.601$ (circled 4). The free surface at this moment is close to the zero-up-crossing level and rising. This evidence highlights a prominent increase of $\{[A_1^*(t^*)]_{gb}\}_{pda}$ and acceleration of the external stream of the generated bore, because the pure bore is ridden by the rising free surface of the 2nd leading wave for $21.455 \leq t^* \leq 21.601$. Figure 19c also shows that the free surface keeps increasing up to the crest level for $t^* = 21.987$ (circled 5), at which the maxima of the non-dimensional free surface elevation and uniform horizontal velocity both occur (see Figures 6b and 8). $\{[A_1^*(t^*)]_{gb}\}_{pda}$, however, decreases rapidly from the maximum value of 0.5403 at $t^* = 21.601$ to 0.0016 at $t^* = 21.987$. This result reveals a continuous decrease in the non-dimensional local accelerations with positive values and successive increase in the non-dimensional uniform horizontal velocity up to the maximum value (0.870) for $21.601 \leq t^* \leq 21.987$. The values of $\{[A_1^*(t^*)]_{gb}\}_{pda}$ are all positive with increasing and decreasing trends for $20.881 \leq t^* \leq 21.455$ and $21.455 \leq t^* \leq 21.987$, respectively. Note that $[u_u^*(t^*)]_{gb}$ always keeps increasing, as evidenced from the velocity profiles marked with the circled 1–5 in Figure 8.
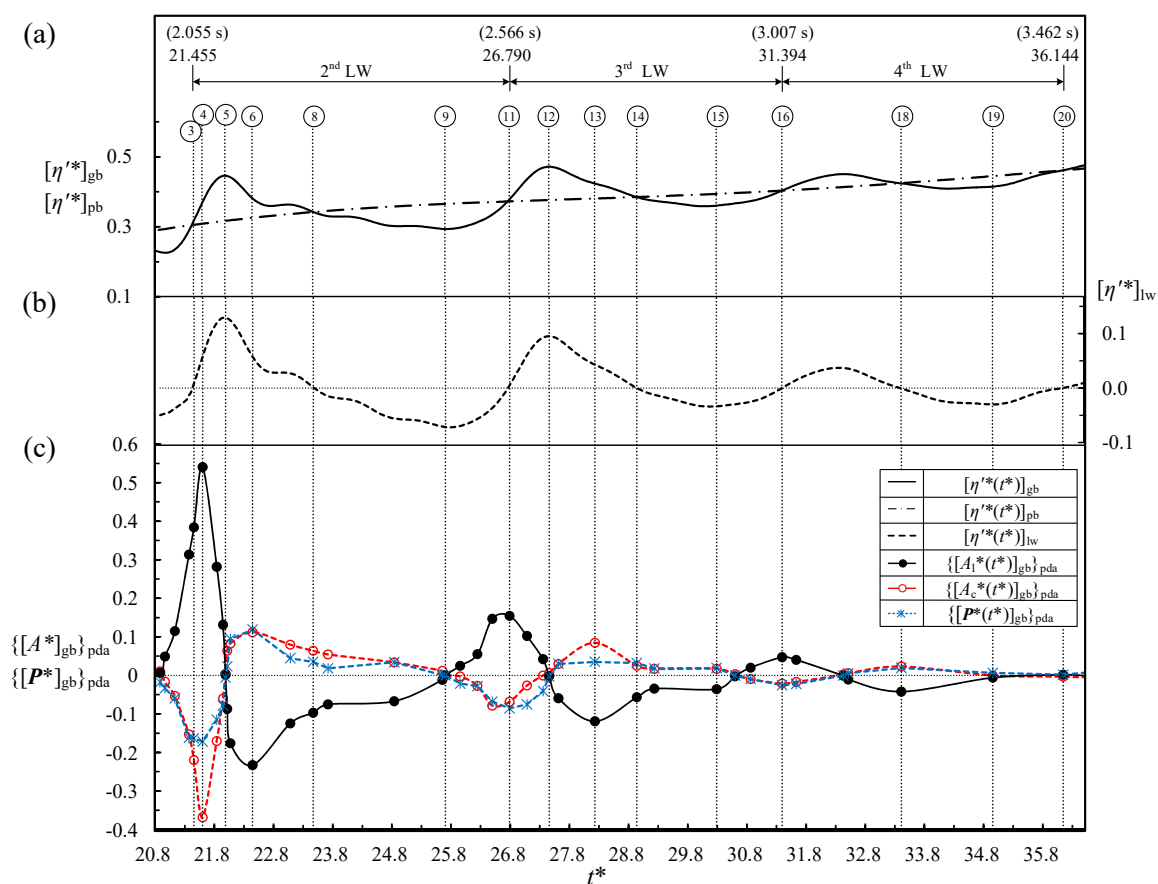

Figure 19. Variations of (**a**) $[\eta'^*(t^*)]_{gb}$ and $[\eta'^*(t^*)]_{pb}$; (**b**) $[\eta'^*(t^*)]_{lw}$; (**c**) $\{[A_1^*(t^*)]_{gb}\}_{pda}$, $\{[A_c^*(t^*)]_{gb}\}_{pda}$, and $\{[P^*(t^*)]_{gb}\}_{pda}$ in onshore direction with t^* for $20.8 \leq t^* \leq 36.5$ at SMS. Times corresponding from circled 3 to 20 are shown in sub-table of Figure 7a,b.

As observed in Figure 19a–c for $21.987 \leq t^* \leq 25.704$, the non-dimensional free surface elevation of the 2nd leading wave undergoes the descending down to the trough level. It varies from the crest level at $t^* = 21.987$, via a specified level at $t^* = 22.447$ and the zero-down-crossing level at around $t^* = 23.470$ (circled 8), then to the second specified level at $t^* = 24.838$, and finally to the trough level at $t^* = 25.704$ (circled 9). Correspondingly, the value of $\{[A_1^*(t^*)]_{gb}\}_{pda}$ changes from 0.0016, via −0.2329 and −0.0970, then to −0.0672, and eventually to 0. The data trend exhibits that prominent deceleration (i.e., $\{[A_1^*(t^*)]_{gb}\}_{pda} < 0$ in the "onshore" direction) of the external stream occurs while the free surface post-passing the crest level and pre-passing the trough level of the 2nd leading wave. Herewith, it is

pertinent to epitomize that the values of $\{[A_1{}^*(t^*)]_{gb}\}_{pda}$ are all negative with magnitudes increasing and decreasing for $21.987 \le t^* \le 22.447$ and $22.447 \le t^* \le 25.704$, respectively. This results in the external stream of the generated bore being continuously decelerated temporally and, consequently, the non-dimensional uniform horizontal velocity $[u_u{}^*(t^*)]_{gb}$ decreasing with the non-dimensional time t^*. The evidences are also observed from the velocity profiles shown in Figure 8 (see the circled 5–9).

In addition, the free surface that experiences the second rising stage of the 2nd leading wave for $25.704 \le t^* \le 26.790$ is between the trough level and the ending phase/zero-up-crossing level of the 2nd/3rd leading wave. During the same non-dimensional time interval, $\{[A_1{}^*(t^*)]_{gb}\}_{pda}$ does increase positively from 0 at $t^* = 25.704$, via 0.0247 at $t^* = 25.955$, then to 0.1544 at $t^* = 26.790$. This trend demonstrates the effect of the second rising in the free surface of the 2nd leading wave on increasing the positive value of $\{[A_1{}^*(t^*)]_{gb}\}_{pda}$. Eventually, this leads to an increase in the magnitude of the non-dimensional uniform horizontal velocity $[u_u{}^*(t^*)]_{gb}$ for the external stream, see the velocity profiles marked with the circled 9–11 in Figure 8.

As estimated by Equations (1) and (8), during the run-up, the non-dimensional onshore uniform horizontal velocity contributed by the "pure bore" is always decelerated (i.e., with negative value of the non-dimensional local acceleration shoreward) before the free-surface peak level is reached at $t^* = 63.623$. However, due to passing of the 2nd leading wave through the SMS for $21.455 \le t^* \le 26.790$, the non-dimensional onshore uniform horizontal velocity of the "generated bore" exhibits drastic variation in the acceleration and deceleration. For example, at the phase soon after the zero-up-crossing level of the 2nd leading wave at $t^* = 21.601$, $\{[A_1{}^*]_{gb}\}_{pda} = 0.5403 >> \{[A_1{}^*]_{pb}\}_{pda} = -0.0204$. In addition, note that, for the phases corresponding to the crest and trough levels of the 2nd leading wave at $t^* = 21.987$ and 25.704, $\{[A_1{}^*]_{gb}\}_{pda} \approx 0$ takes place, however, $\{[A_1{}^*]_{pb}\}_{pda} = [A_1{}^*]_{pb} = -0.0203$ and -0.0193 occur, respectively.

6.2.2. Influences of 3rd and 4th Leading Waves

The time intervals for $26.790 \le t^* \le 31.394$ and $31.394 \le t^* \le 36.144$ correspond to passing of the 3rd and 4th leading waves through the SMS. During one of the two time intervals, the variation features of $\{[A_1{}^*(t^*)]_{gb}\}_{pda}$ and $[u_u{}^*(t^*)]_{gb}$ are fairly similar to those illustrated for the 2nd leading wave but with decreasing magnitudes in the positive and negative extrema of $\{[A_1{}^*(t^*)]_{gb}\}_{pda}$ and in $[u_u{}^*(t^*)]_{gb}$. For example, the value of $\{[A_1{}^*(t^*)]_{gb}\}_{pda}$ equal to 0 still occurs around the instants for the crest and trough levels of the 3rd and 4th leading waves. This is because the highest/lowest water level is reached for the crest/trough phase, at which the positive/negative maximum of the non-dimensional horizontal velocity occurs. The positive and negative extrema of $\{[A_1{}^*(t^*)]_{gb}\}_{pda}$ for the 3rd leading wave take the values of 0.1544 for $t^* = 26.790$ (i.e., at the zero-up-crossing phase) and -0.1195 at $t^* = 28.231$ (at the descending stage after the crest phase), respectively. The counterparts for the 4th leading wave have the values of 0.0469 at $t^* = 31.394$ and -0.0422 at $t^* = 33.410$, respectively. All the data show nearly identical phases to those of the 2nd leading wave. These results do show decreasing influence of the 3rd and 4th leading waves on $\{[A_1{}^*(t^*)]_{gb}\}_{pda}$ and $[u_u{}^*(t^*)]_{gb}$ (see the circled 11–20 in Figure 8).

6.2.3. No Influence of Leading Wave for $36.144 \le t^* < 125.284$

As confirmed in Section 4.2, the free surface variation of the kth leading wave (with $k \ge 5$) has little effect (see Figure 10) on the velocity shift. This allows one to neglect its effect on the velocity distribution of the generated bore during the run-up. Whether such a minor velocity shift has any effect on the local acceleration should be examined.

The positive and negative extrema of $\{[A_1{}^*(t^*)]_{gb}\}_{pda}$ for the 5th leading wave are equal to 0.0015 for $t^* = 36.144$ (i.e., $t = 3.462$ s, at the zero-up-crossing phase, circled 20) and -0.0216 at $t^* = 38.744$ (i.e., $t = 3.711$ s, at the zero-up-crossing phase, circled 23). These two relative magnitudes with respect to the positive maximum of the 2nd leading wave (0.5403) are as small as 0.3% and 4.0%. For both the 6th and 7th leading waves, all the relative magnitudes are much lower than 2.0% (not shown), indicating

that their tiny contribution can be neglected. Accordingly, the non-dimensional local acceleration is justified to be nearly contributed by the pure bore, i.e., $\{[A_1^*(t^*)]_{gb}\}_{pda} \approx \{[A_1^*(t^*)]_{pb}\}_{pda}$ for $t^* > 36.144$.

During the run-up for $36.144 \leq t^* \leq 63.623$, $\{[A_1^*(t^*)]_{gb}\}_{pda}$ is approximately equal to $\{[A_1^*(t^*)]_{pb}\}_{pda}$ (see Figure 20a,b), thus being expressed as:

$$\{[A_1^*(t^*)]_{gb}\}_{pda} \approx \{[A_1^*(t^*)]_{pb}\}_{pda} = [A_1^*(t^*)]_{pb} = \partial[u_u^*(t^*)]_{pb}/\partial t^*$$
$$= -0.0222 \times \exp[-0.0137(t^* - 15.243)] \quad \text{for } 36.144 \leq t^* \leq 63.623. \tag{10}$$

Equation (10) justifies deceleration of the generated (or pure) bore with temporally exponential decay trend in the onshore direction during the run-up. For example, $\{[A_1^*]_{gb}\}_{pda} \approx [A_1^*(t^*)]_{pb} = -0.0206, -0.0167, -0.0138$, and -0.0115 at $t^* = 20.881, 36.144, 50.343$, and 63.623, respectively.

Moreover, during the run-down for $63.623 \leq t^* < 125.284$ (without existence of any leading wave), $\{[A_1^*(t^*)]_{gb}\}_{pda}$ is equal to $\{[A_1^*(t^*)]_{pb}\}_{pda} = [A_1^*(t^*)]_{pb} = \partial[u_u^*(t^*)]_{pb}/\partial t^*$ (see Equation (9)):

$$\{[A_1^*(t^*)]_{gb}\}_{pda} = [A_1^*(t^*)]_{pb} = -0.0115 \quad \text{for } 63.623 \leq t^* < 125.284. \tag{11}$$

Equation (11) reconfirms the non-dimensional local acceleration of the generated (or pure) bore with a constant value of 0.0115 in the offshore direction during the run-down for $63.623 \leq t^* < 125.284$, demonstrating increase in $[u_u^*(t^*)]_{pb}$ with t^*.
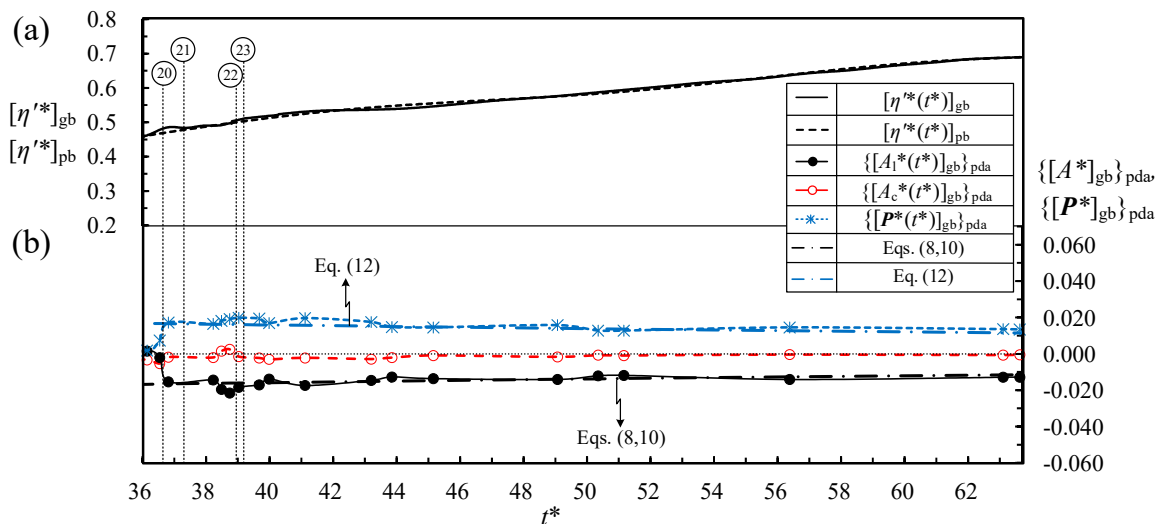

Figure 20. Variations of (**a**) $[\eta'^*(t^*)]_{gb}$ and $[\eta'^*(t^*)]_{pb}$; (**b**) $\{[A_1^*(t^*)]_{gb}\}_{pda}$, $\{[A_c^*(t^*)]_{gb}\}_{pda}$ and $\{[P^*(t^*)]_{gb}\}_{pda}$ in onshore direction with t^* for $36.0 \leq t^* \leq 63.70$ at SMS. Note that $[A_1^*(t^*)]_{pb}$ and $[P^*(t^*)]_{pb}$, are also included and vertical scale is 10 times smaller than that of Figure 19c. Times range from circled 20 to 23 are listed in sub-table of Figure 7a,b.

6.3. Convective Acceleration of Generated Bore at SMS

6.3.1. Influence of 2nd Leading Wave

Figure 19c also shows variation of $\{[A_c^*(t^*)]_{gb}\}_{pda}$ ($=\{[A_{c1}^*(t^*)]_{gb}\}_{pda} + \{[A_{c2}^*(t^*)]_{gb}\}_{pda} = \{[u^*(t^*) \times \partial u^*(t^*)/\partial x^*]_{gb}\}_{pda} + \{[v^*(t^*) \times \partial u^*(t^*)/\partial y^*]_{gb}\}_{pda}$) with t^*, obtained at the SMS. The value of $\{[A_c^*(t^*)]_{gb}\}_{pda}$ varies from -0.0166 for $t^* = 20.964$, via -0.1532 and -0.2200 for $t^* = 21.371$ and 21.455, down to the negative maximum of -0.3686 for $t^* = 21.601$. Right at the latter instant, the positive maximum of $\{[A_1^*(t^*)]_{gb}\}_{pda}$ occurs just during the first rising stage soon after the zero-up-crossing phase of the 2nd leading wave. The value of $\{[A_c^*(t^*)]_{gb}\}_{pda}$ changes from the negative maximum ($=-0.3686$) for $t^* = 21.601$, via -0.1704 for $t^* = 21.841$, up to 0.0043 for $t^* = 21.987$, at which the free surface of the 2nd leading wave reaches the crest level and $\{[A_c^*(t^*)]_{gb}\}_{pda}$ is very close to zero.

As mentioned above, the entire descending stage of the 2nd leading wave extends from the crest level, via the zero-down-crossing level, down to the trough level. $\{[A_c^*(t^*)]_{gb}\}_{pda}$ subsequently ranges from 0.0043 for $t^* = 21.987$ at the crest phase, via 0.0639 for $t^* = 22.019$ and the positive maximum of 0.1119 for $t^* = 22.447$ (where $\{[A_l^*(t^*)]_{gb}\}_{pda}$ has the negative maximum), then down to 0.0638 for $t^* = 23.470$ (i.e., at the zero-down-crossing level) and 0 for $t^* = 25.704$ (i.e., at the trough level). Finally, during the second rising stage between the trough level and ending phase of the 2nd leading wave, the value of $\{[A_c^*(t^*)]_{gb}\}_{pda}$ varies from 0 for $t^* = 25.704$, via -0.0029 for $t^* = 25.955$ and -0.0271 for $t^* = 26.247$, down to -0.0686 for $t^* = 26.790$.

Based on the definition of the convective acceleration, the term $[u(x, y, t) \times \partial u(x, y, t)/\partial x]_{gb}$, is expected to play a more important role than $[v(x, y, t) \times \partial u(x, y, t)/\partial y]_{gb}$, as seen in Tables A2 and A3 in Appendix B. At $t^* = 21.987$, the crest of the 2nd leading wave exactly passes through the SMS (Figure 7). At this instant, the free surface profile with the crest at the SMS has a relatively symmetric form covering the region $21.22 \leq x^* \leq 21.92$ (191.0 cm $\leq x \leq$ 197.3 cm) (see Figure 6b). The maximum horizontal velocity profile $([u^*(y^*)]_{gb})_{max}$ underneath the crest exists at the SMS for $t^* = 21.987$. However, for the crest of the 2nd leading wave pre-passing and post-passing the SMS (see Figure 6a,c), the actual position for the crest and the maximum horizontal velocity profile should appear for $x^* < 21.56$ and $t^* < 21.987$ as well as for $x^* > 21.56$ and $t^* > 21.987$, respectively. This leads to the negative and positive values of the convective acceleration for $20.881 \leq t^* < 21.987$ (during the first rising stage) and $20.987 \leq t^* < 25.704$ (during the entire descending stage), respectively. The horizontal velocity gradients take negative and positive values for the former and latter intervals, respectively. Further, during the second rising stage for $25.704 \leq t^* < 26.790$, the crest of the 3rd leading wave approaches the SMS (at which passing of the crest of the 3rd leading wave occurs at $t^* = 27.458$). This is similar to that illustrated for the 2nd leading wave for $t^* < 21.987$ (i.e., pre-passing of the 3rd leading-wave crest results in $[u^*\partial u^*/\partial x^*]_{gb} < 0$), thus rendering the convective acceleration to be negative, as evidenced in Figure 19c.

6.3.2. Influences of 3rd and 4th Leading Waves

Within the intervals for $26.790 \leq t^* \leq 31.394$ and $31.394 \leq t^* \leq 36.144$ (corresponding to passing of the 3rd and 4th leading waves through the SMS), the variation trends of $\{[A_c^*(t^*)]_{gb}\}_{pda}$ are similar to those for the 2nd leading wave but with decreasing magnitude of the positive and negative extrema. Taking the 3rd leading wave for example, the negative and positive extrema of $\{[A_c^*(t^*)]_{gb}\}_{pda}$ are equal to -0.0686 at $t^* = 26.790$ and 0.0845 at $t^* = 28.231$. The counterparts of $\{[A_c^*(t^*)]_{gb}\}_{pda}$ for the 4th leading wave hold the values of -0.0215 at $t^* = 31.394$ and 0.0229 at $t^* = 33.409$, respectively.

6.3.3. No Influence of Leading Wave for $36.144 \leq t^* < 125.284$

The 5th leading wave takes place for $36.144 \leq t^* < 38.744$, the negative and positive maxima of $\{[A_c^*(t^*)]_{gb}\}_{pda}$ are -0.0053 at $t^* = 36.541$ and 0.0025 at $t^* = 38.744$. The relative deviations of the two magnitudes (with reference to the positive maximum of the local acceleration of the 2nd leading wave, i.e., $\{[A_l^*(t^*)]_{gb}\}_{pda} = 0.5403$) amount to 1.0% and 0.5%. This fact reveals that the corresponding contributions from the 5th leading wave are much smaller, and their effects can be neglected. Afterwards, the partially depth-averaged value of the non-dimensional convective acceleration is regarded as being mostly contributed by the external stream of the pure bore, i.e., $\{[A_c^*(t^*)]_{gb}\}_{pda} \approx \{[A_c^*(t^*)]_{pb}\}_{pda}$ for $t^* > 36.144$. Further, this allows $\{[A_c^*(t^*)]_{gb}\}_{pda}$ to be determined by $\{[u^*(t^*) \times \partial u^*(t^*)/\partial x^*]_{pb}\}_{pda}$, because the minor effect or lacking of leading waves as well as the uniform horizontal velocity of pure bore being constant in the y^* direction (i.e., $[\partial u^*(t^*)/\partial y^*]_{gb} \approx [\partial u_u^*(t^*)/\partial y^*]_{pb} = 0$) are all evidenced. Based on the velocity fields, the values of $\{[A_c^*(t^*)]_{gb}\}_{pda}$ are calculated to be around $\pm O(10^{-3})$ (not shown) for $36.144 \leq t^* < 125.284$. They are far smaller than the positive maximum of $\{[A_l^*(t^*)]_{gb}\}_{pda}$ (=0.5403) for the 2nd leading wave and thus neglected hereafter.

6.4. Pressure Gradient of Generated Bore at SMS

6.4.1. Influence of Leading Waves

From Equation (5), the partially depth-averaged value of the non-dimensional pressure gradient in the external stream of generated bore, $\{[P^*]_{gb}\}_{pda}$, is equal to $-\{[A_t^*(t^*)]_{gb}\}_{pda} = -(\{[A_1^*(t^*)]_{gb}\}_{pda} + \{[A_c^*(t^*)]_{gb}\}_{pda})$. The positive/negative value of the pressure gradient, which is termed adverse/favorable pressure gradient, identifies deceleration/acceleration of the external stream in the onshore direction.

Figure 19c also illustrates variation of $\{[P^*(t^*)]_{gb}\}_{pda}$ with t^* and its relationship with the counterparts of $\{[A_1^*(t^*)]_{gb}\}_{pda}$ and $\{[A_c^*(t^*)]_{gb}\}_{pda}$ at the SMS. The variation trend of $\{[P^*(t^*)]_{gb}\}_{pda}$ is similar to that of $\{[A_c^*(t^*)]_{gb}\}_{pda}$. During the first rising stage from the zero-up-crossing to the crest level of the 2nd leading wave for $21.455 \leq t^* \leq 21.987$, the values of $\{[P^*(t^*)]_{gb}\}_{pda}$ and $\{[A_1^*(t^*)]_{gb}\}_{pda}$ are all negative and positive, together with the negative and positive extrema of -0.1717 and 0.5403 occurring at $t^* = 21.601$. These data reveal that the external stream of the bore is accelerated both spatially and temporally in the onshore direction under the favorable pressure gradient due to pre-passing of the crest for the 2nd leading wave at the SMS for $21.455 \leq t^* < 21.987$. At the crest level of the 2nd leading wave for $t^* = 21.987$, the values of $\{[P^*]_{gb}\}_{pda}$, $\{[A_1^*]_{gb}\}_{pda}$ and $\{[A_c^*]_{gb}\}_{pda}$ are very close to 0. This indicates that the external stream of generated bore is instantaneously almost under zero pressure gradient with $\{[A_t^*]_{gb}\}_{pda} = 0$.

During the descending stage from the crest to trough level of the 2nd leading wave for $21.987 < t^* < 25.704$, the values of $\{[P^*(t^*)]_{gb}\}_{pda}$ and $\{[A_1^*(t^*)]_{gb}\}_{pda}$ are all positive and negative, along with the positive and negative extrema of 0.1189 and -0.2329 occurring at $t^* = 22.447$ (see Figure 19c). The trend demonstrates that the external stream of generated bore is decelerated both spatially and temporally in the onshore direction under adverse pressure gradient due to post-passing of the crest of the 2nd leading wave at the SMS for $21.987 < t^* < 25.704$. At the trough level for $t^* = 25.704$, the values of $\{[P^*]_{gb}\}_{pda}$, $\{[A_1^*]_{gb}\}_{pda}$ and $\{[A_c^*]_{gb}\}_{pda}$ are equal or very close to 0. The fact indicates that the generated bore is instantaneously nearly under zero pressure gradient, together with the non-dimensional local and convective accelerations equal to 0 at $t^* = 25.704$.

During the second rising stage from the trough level of the 2nd leading wave to the zero-up-crossing level of the 3rd one for $25.704 \leq t^* \leq 26.790$, the value of $\{[P^*]_{gb}\}_{pda}$ decreases from nearly 0 to the local negative maximum of -0.0858, together with increase in the positive value of $\{[A_1^*]_{gb}\}_{pda}$ (Figure 19c). The external stream of the generated bore, which is subject to the favorable pressure gradient, is accelerated spatially and temporally for $25.704 \leq t^* \leq 26.790$. A complete chronology of variations both in the pressure gradient (from favorable, via zero, to adverse pressure gradient) and in the flow situation (from positive, via zero, to negative local acceleration) from the first rising stage up to the crest phase, via the entire descending stage, then to the second rising stage of the 2nd leading wave is thus outlined.

Figure 19c also shows that the features of variations in $\{[P^*(t^*)]_{gb}\}_{pda}$, $\{[A_1^*(t^*)]_{gb}\}_{pda}$, and $\{[A_c^*(t^*)]_{gb}\}_{pda}$ abovementioned also happen for the 3rd and 4th leading waves. For example, from the zero-up-crossing to the crest level of the 3rd leading wave for $26.790 \leq t^* \leq 27.458$, the values of $\{[P^*(t^*)]_{gb}\}_{pda}$ and $\{[A_1^*(t^*)]_{gb}\}_{pda}$ are all negative and positive, along with the negative and positive extrema of -0.0858 and 0.1544 taking place at $t^* = 26.790$. Next, very close to the crest/trough level of the 3rd leading wave at $t^* = 27.458/30.590$, the values of $\{[P^*]_{gb}\}_{pda}$, $\{[A_1^*]_{gb}\}_{pda}$ and $\{[A_c^*]_{gb}\}_{pda}$ are nearly equal to 0. At the ending/zero-up-crossing phase of the 3rd/4th leading wave for $t^* = 31.394$, the values of $\{[P^*]_{gb}\}_{pda}$ and $\{[A_1^*]_{gb}\}_{pda}$ are equivalent to a negative maximum of -0.0255 and a positive maximum of 0.0469. It can be summarized that the magnitudes of the negative maximum of $\{[P^*]_{gb}\}_{pda}$ and the positive maximum of $\{[A_1^*]_{gb}\}_{pda}$ both decrease with increasing "n" of the nth leading wave (for $n = 2$–4).

6.4.2. No Influence of Leading Wave

As seen in Figure 20a,b for the ending/zero-up-crossing phase of the 4th/5th leading wave at $t^* = 36.144$ ($t = 3.462$ s), the values of $\{[P^*]_{\mathrm{gb}}\}_{\mathrm{pda}}$ and $\{[A_1^*]_{\mathrm{gb}}\}_{\mathrm{pda}}$ are equivalent to 0.0019 and 0.0015, along with $\{[A_\mathrm{c}^*]_{\mathrm{gb}}\}_{\mathrm{pda}} = -0.0033$. The relative deviations of the magnitude is equal to 0.4% and 0.3% (with respect to the positive maximum of $\{[A_1^*]_{\mathrm{gb}}\}_{\mathrm{pda}} = 0.5403$ for the 2nd leading wave). The result demonstrates that the two associated values of the 5th leading wave, $\{[P^*]_{\mathrm{gb}}\}_{\mathrm{pda}}$ and $\{[A_1^*]_{\mathrm{gb}}\}_{\mathrm{pda}}$, for $36.144 \leq t \leq 38.744$ are much smaller than those of the 2nd leading wave. Up to now, the remaining kth leading waves (with $k \geq 5$) has been demonstrated to play a less or minute role on the velocity shift as well as the contribution to accelerations, thus resulting in the generated bore almost being contributed by the pure bore.

As illustrated in Section 6.3, the values of $\{[A_\mathrm{c}^*(t^*)]_{\mathrm{gb}}\}_{\mathrm{pda}}$ are shown to be only around O(10^{-3}). The values are so small and can thus be neglected hereafter for $36.144 \leq t^* < 125.284$. Based on Equations (5), (8), and (10) for $36.144 \leq t^* \leq 63.623$, the partially depth-averaged value of the non-dimensional pressure gradient of the generated (or pure) bore in the onshore direction can be determined by:

$$
\begin{aligned}
\{[P^*(t^*)]_{\mathrm{gb}}\}_{\mathrm{pda}} &= [P^*(t^*)]_{\mathrm{pb}} \\
&= -[A_1^*(t^*)]_{\mathrm{pb}} = -[\partial u_\mathrm{u}^*(t^*)/\partial t^*]_{\mathrm{pb}} \\
&= 0.0222 \times \exp[-0.0137(t^* - 15.243)] \quad \text{for } 36.144 \leq t^* \leq 63.623.
\end{aligned}
\tag{12}
$$

The feature indicates that, during the run-up for $36.144 \leq t^* \leq 63.623$, persistent deceleration of the external stream of the pure bore keeps undergoing shoreward under the adverse pressure gradient with decreasing magnitude, as shown in Figure 21a,b.
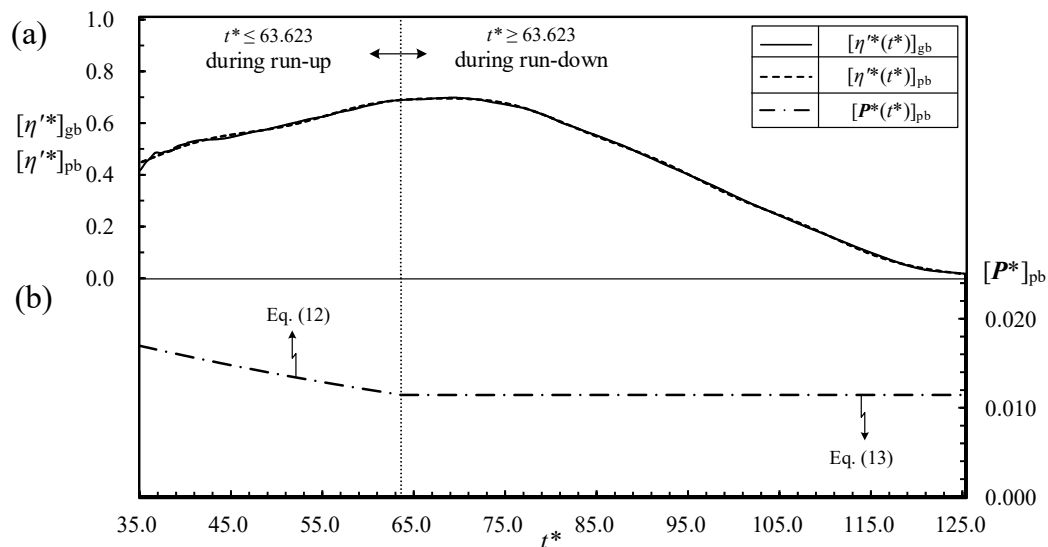

Figure 21. Variations of (**a**) $[\eta'^*(t^*)]_{\mathrm{gb}}$ and $[\eta'^*(t^*)]_{\mathrm{pb}}$; (**b**) $[P^*(t^*)]_{\mathrm{pb}}$ with t^* during run-up and run-down for $35.0 \leq t^* \leq 63.623$ and $63.623 \leq t^* < 125.284$, respectively.

From Equations (5), (9), and (11) for $63.623 \leq t^* < 125.284$, the partially depth-averaged value of the non-dimensional pressure gradient of the generated (or pure) bore in the onshore direction is obtained:

$$
\begin{aligned}
\{[P^*(t^*)]_{\mathrm{gb}}\}_{\mathrm{pda}} &= [P^*(t^*)]_{\mathrm{pb}} \\
&= -[A_1^*(t^*)]_{\mathrm{pb}} = -[\partial u_\mathrm{u}^*(t^*)/\partial t^*]_{\mathrm{pb}} \\
&= 0.0115 \quad \text{for } 63.623 \leq t^* < 125.284,
\end{aligned}
\tag{13}
$$

namely, $-\{[P^*]_{\mathrm{gb}}\}_{\mathrm{pda}} = -[P^*]_{\mathrm{pb}} = -0.0115$ is negative in the offshore direction. The fact exhibits that, during the run-down for $63.623 \leq t^* < 125.284$, the external stream of the generated bore (or pure bore) is accelerated in the offshore direction under a non-dimensional favorable pressure gradient of -0.0115. This fact is also illustrated in Figure 21a,b, together with the non-dimensional free surface elevation displayed for $36.144 \leq t^* < 125.284$.

6.5. Systematic Summary of Procedure for Exploring Features of Accelerations and Pressure Gradient

To achieve a complete understanding for the features of accelerations and pressure gradients of the generated and pure bores, a systematic summary of the frame structure for different steps is illustrated through the flow chart shown in Figure 22. Note that the relationships among the free surface elevations, velocities, accelerations, and pressure gradients of the pure bore and generated bore are highlighted. The sections/subsections/equations corresponding to a specified working item are also included for reference. It is expected that the flow chart can be used as a guideline for further studies on the undular bores with different values of h_1/h_0 and propagating on sloping beaches with distinct slopes.
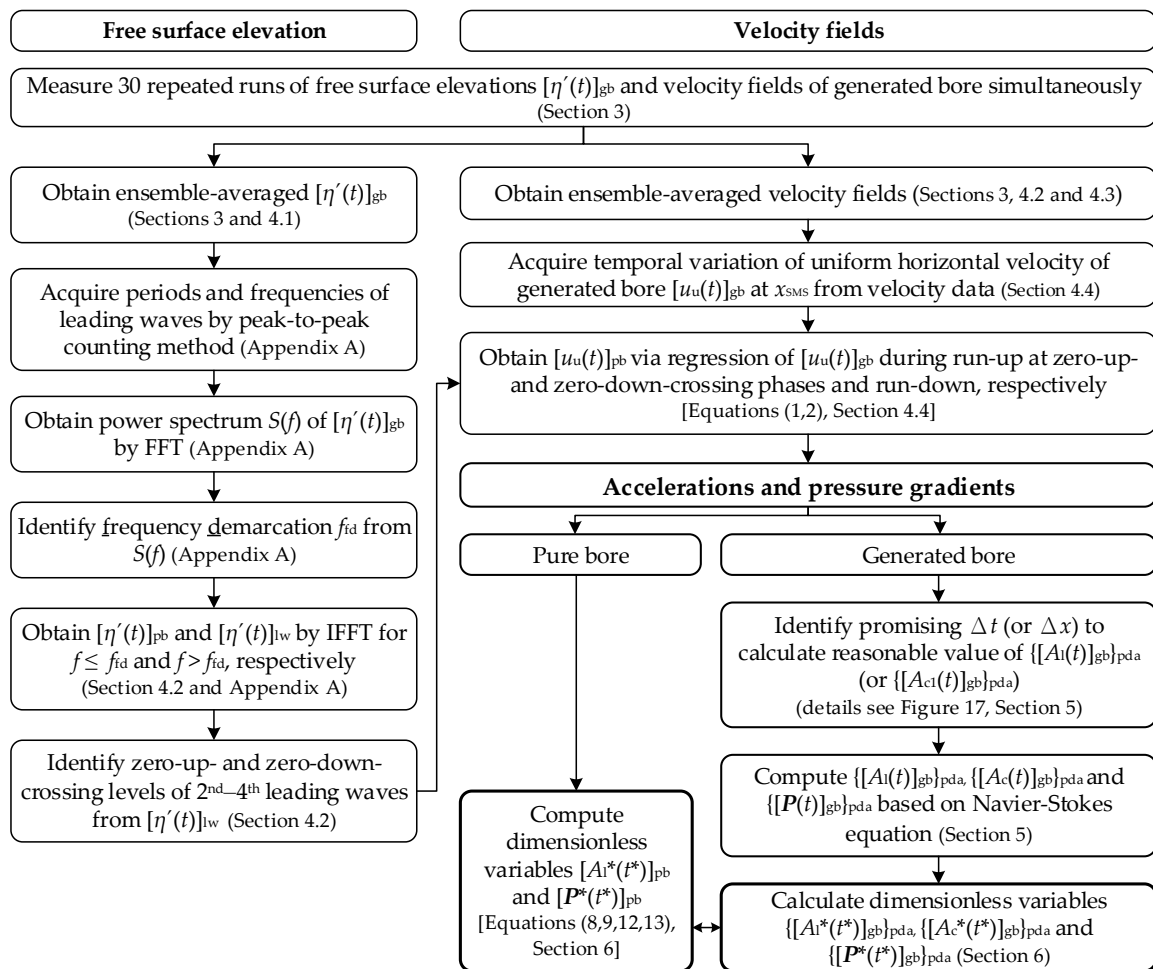
Figure 22. Flow chart systematically illustrating relationships among free surface elevations, velocities, accelerations, and pressure gradients of pure and generated bores.

7. Concluding Remarks

The HSPIV experimental results on the characteristics of both velocity fields and accelerations as well as pressure gradient in the horizontal direction for the external stream of a dambreak-generated undular bore (with $h_1/h_0 = 1.70$), propagating over a 1:20 sloping beach during the run-up and run-down, were presented. Major findings can be drawn as follows:

1. The 1st leading wave breaks at $x^* = x_{bp1}/h_0 = 11.3$ for $t^* = 8.728$, leading to the dissipation of energy due to lifting motion of air bubbles under a bubbly turbulent flow. Under such a situation, rise in the free surface elevation of the 1st leading wave no longer exists. Instead, a plateau-shaped

free surface with some small-scale wavy oscillations in the time series of $[\eta'^*(t^*)]_{gb}$ is observed for $16.182 < t^* < 21.455$ prior to arrival of the 2nd leading wave at the SMS for $x^* = 21.56$.

2. During the run-up for $20.881 \leq t^* \leq 63.623$, variations of $[u_u^*(t^*)]_{pb}$ and $[A_1^*(t^*)]_{pb}$ with t^* for the pure bore are presented by Equations (6) and (8), respectively. The trends exhibit the successive decrease in the non-dimensional (onshore) uniform horizontal velocity and continuous deceleration of the pure bore in the onshore direction. However, the pure bore accompanied by the leading waves is decelerated/accelerated spatially and accelerated/decelerated temporally in the onshore direction during the rising/descending free surface of the nth (with $n = 2$–4) leading wave. This demonstrates the effect of pre-passing/post-passing of the leading wave crest on the velocity distribution of generated bore. On the other hand, during the run-down for $63.623 \leq t^* < 125.2843$, variations of $[u_u^*(t^*)]_{pb}$ and $[A_1^*(t^*)]_{pb}$ with t^* are expressed by Equations (7) and (9), respectively. Both trends highlight the magnitude of the non-dimensional (offshore) uniform horizontal velocity increasing linearly and the non-dimensional local acceleration being constant (0.0115 in the offshore direction) with increasing non-dimensional time.

3. In the course of the first rising stage of the 2nd leading wave, the values of $\{[A_1^*(t^*)]_{gb}\}_{pda}$ are all positive with increasing/decreasing trend for $21.455 \leq t^* \leq 21.601/21.601 \leq t^* < 21.987$, respectively. A positive maximum of 0.5403 takes place at $t^* = 21.601$ soon after the zero-up-crossing phase and 0 at $t^* = 21.987$ for the crest level of the 2nd leading wave. This evidence reveals continuous acceleration of the external stream of the generated bore in the onshore direction.

4. During the descending stage of the 2nd leading wave for $21.987 \leq t^* \leq 22.447$ and $22.447 \leq t^* \leq 25.704$, the values of $\{[A_1^*(t^*)]_{gb}\}_{pda}$ are all negative with the increasing and decreasing magnitudes, respectively. A negative maximum of -0.2329 appears at $t^* = 22.447$ after the crest phase and 0 at $t^* = 25.704$ for the trough phase. This situation results in the external stream being decelerated temporally. Further with the second rising stage of the 2nd leading wave for $25.704 \leq t^* \leq 26.790$, $\{[A_1^*(t^*)]_{gb}\}_{pda}$ increases positively from 0 at $t^* = 25.704$ for the trough phase, to 0.1544 at $t^* = 26.790$ for the ending/zero-up-crossing phase of the 2nd/3rd leading wave. This trend demonstrates the effect of the second rising in the free surface on increasing the values of both $\{[A_1^*(t^*)]_{gb}\}_{pda}$ and $[u_u^*(t^*)]_{gb}$ of the external stream of the generated bore.

5. With passing of the 3rd and 4th leading waves, respectively, for $26.790 \leq t^* \leq 31.394$ and $31.394 \leq t^* \leq 36.144$, the variation feature in $\{[A_1^*(t^*)]_{gb}\}_{pda}$ is fairly similar to that for the 2nd leading wave but with decreasing magnitudes in the positive and negative extrema of $\{[A_1^*(t^*)]_{gb}\}_{pda}$. Moreover, the contributions from the kth leading wave (with $k \geq 5$) are much smaller and their influences can be neglected. Afterwards, the non-dimensional local acceleration of the external stream of the generated bore can be regarded as being nearly contributed only by the pure bore, i.e., $\{[A_1^*(t^*)]_{gb}\}_{pda} \approx \{[A_1^*(t^*)]_{pb}\}_{pda} = [A_1^*(t^*)]_{pb}$ for $t^* > 36.144$.

6. Furthermore, for the run-up with $36.144 < t^* \leq 63.623$, $\{[A_1^*(t^*)]_{gb}\}_{pda}$ is approximately equal to $[A_1^*(t^*)]_{pb}$ (i.e., Equation (8)), clearly justifying deceleration of the generated (or pure) bore with temporally exponential decay trend in the onshore direction. Moreover, during the run-down for $63.623 \leq t^* < 125.284$, $\{[A_1^*(t^*)]_{gb}\}_{pda}$ amounts to $[A_1^*(t^*)]_{pb} = -0.0115$ (i.e., Equation (9)), revealing a constant acceleration of the pure bore in the offshore direction and increase of the offshore uniform horizontal velocity with time.

7. The non-dimensional (onshore) uniform horizontal velocity, contributed by the "pure bore" during the run-up, is always decelerated due to the negative value of the non-dimensional local acceleration shoreward before arrival of the free-surface peak level of the pure bore at $t^* = 63.623$. However, due to passing of the nth leading wave for $21.455 \leq t^* \leq 36.144$, the non-dimensional onshore uniform horizontal velocity of the "generated bore" exhibits drastic variation in flow acceleration and deceleration in the horizontal direction. The most striking influence of the velocity shift on the non-dimensional local acceleration of the generated bore is evidenced at the phase soon after the zero-up-crossing level of the 2nd leading wave. Namely, at $t^* = 21.601$, $\{[A_1^*]_{gb}\}_{pda}$ of the generated bore is equal to 0.5403, far larger than that ($\{[A_1^*]_{pb}\}_{pda} = [A_1^*]_{pb} =$

−0.0204) of the pure bore. Similar qualitative features are also experienced for the 3rd and 4th leading waves but with evident decreasing magnitudes.

8.　During the first rising stage of the 2nd leading wave $21.455 \leq t^* \leq 21.987$, the value of $\{[A_c^*(t^*)]_{gb}\}_{pda}$ varies from −0.2200 via −0.3686 (negative maximum), −0.1704 to 0.0043 respectively at $t^* = 21.455$ (for zero-up-crossing phase), 21.601 (soon after the zero-up-crossing phase), 21.841 to 21.987 (for the crest phase). For the entire descending stage for $21.987 \leq t^* \leq 25.704$, $\{[A_c^*(t^*)]_{gb}\}_{pda}$ ranges from 0.0043, via 0.1119 (positive maximum), to 0 at $t^* = 21.987$, 22.447 to 25.704 for the trough level. Moreover, during the second rising stage, the value of $\{[A_c^*(t^*)]_{gb}\}_{pda}$ varies from 0, via −0.0271 for $t^* = 26.247$, down to −0.0686 for $t^* = 26.790$. Pre-passing and post-passing of the 2nd leading-wave crest renders $\{[A_c^*(t^*)]_{gb}\}_{pda}$ to be negative and positive, respectively. Similar features are also observed for the 3rd and 4th leading waves but with decreasing magnitudes. However, the contribution from the kth leading wave (with $k \geq 5$) to $\{[A_c^*(t^*)]_{gb}\}_{pda}$ is much smaller and their effects can be neglected. Afterwards, the non-dimensional convective acceleration can be regarded as being mostly contributed by the external stream of the pure bore for $t^* > 36.144$. Due to very minor effect or lacking of the leading waves as well as the non-dimensional uniform horizontal velocity of pure bore being constant in the y^* direction ($[\partial u_u^*(t^*)/\partial y^*]_{pb} = 0$), the values of $\{[A_c^*(t^*)]_{gb}\}_{pda}$ are eventually found to be around $\pm O(10^{-3})$ for $36.144 < t^* < 125.284$. The values are far smaller than the positive maximum of the non-dimensional local acceleration of the 2nd leading wave ($\{[A_l^*(t^*)]_{gb}\}_{pda} = 0.5403$ at $t^* = 21.601$) and thus their influences are ignored.

9.　Additionally, for the first rising stage of the 2nd leading wave with $21.455 < t^* < 21.987$, the values of $\{[P^*]_{gb}\}_{pda}$ and $\{[A_l^*]_{gb}\}_{pda}$ are all negative and positive, with their extrema of −0.1717 and 0.5403 occurring at $t^* = 21.601$. This reveals that the external stream is accelerated both spatially and temporally in the onshore direction under the favorable pressure gradient due to pre-passing of the crest for the 2nd leading wave. At $t^* = 21.987$ for the crest phase, the values of $\{[P^*]_{gb}\}_{pda}$, $\{[A_l^*]_{gb}\}_{pda}$ and $\{[A_c^*]_{gb}\}_{pda}$ are very close to 0. This feature highlights the external stream is instantaneously almost under zero pressure gradient.

10.　During the descending stage of the 2nd leading wave for $21.987 < t^* < 25.704$, the values of $\{[P^*]_{gb}\}_{pda}$ and $\{[A_l^*]_{gb}\}_{pda}$ are all positive and negative, respectively, along with the positive and negative extrema of 0.1189 and −0.2329 occurring at $t^* = 22.447$. The trend justifies that the external stream is decelerated both spatially and temporally in the onshore direction under adverse pressure gradient due to post-passing of the 2nd leading wave crest for $21.987 < t^* < 25.704$. Exactly at the trough level for $t^* = 25.704$, the values of $\{[P^*]_{gb}\}_{pda}$, $\{[A_l^*]_{gb}\}_{pda}$ and $\{[A_c^*]_{gb}\}_{pda}$ are equal or very close to 0. The fact indicates that the generated bore is instantaneously nearly under zero pressure gradient, together with the non-dimensional local and convective accelerations equal to 0 at $t^* = 25.704$ for the trough phase.

11.　Further, during the second rising stage of the 2nd leading wave for $25.704 < t^* < 26.790$, the value of $\{[P^*]_{gb}\}_{pda}$ decreases from nearly 0 to the local negative maximum of −0.0857, together with increase in the positive value of $\{[A_l^*]_{gb}\}_{pda}$. Therefore, the external stream of generated bore subject to the favorable pressure gradient is accelerated spatially and temporally. A similar feature of the temporal variation in $\{[P^*]_{gb}\}_{pda}$ occurs for the 3rd and 4th leading waves but all with decreasing magnitudes for $26.790 \leq t^* \leq 36.144$. Additionally, the remaining kth leading wave (with $k \geq 5$) plays little role on the non-dimensional convective acceleration for $t^* > 36.144$, thus the influence can be neglected.

12.　In addition, for the run-up with $36.144 \leq t^* \leq 63.623$, the variation of $\{[P^*]_{gb}\}_{pda}$ with t^* indicates that deceleration of the external stream of the generated (or pure) bore keeps undergoing shoreward under the adverse pressure gradient with decreasing magnitude as expressed by Equation (12). However, during the run-down for $63.623 \leq t^* < 125.284$, $\{[P^*]_{gb}\}_{pda}$ is equal to 0.0115 in the onshore direction, i.e., $-\{[P^*]_{gb}\}_{pda} = -0.0115$ (Equation (13)), being negative in the offshore direction. This result demonstrates that the external stream of the generated bore (or

pure bore) is accelerated in the offshore direction with a non-dimensional acceleration of 0.0115 and under a non-dimensional favorable pressure gradient of −0.0115.

Finally, two integrated flow charts (Figures 17 and 22), which address the frame structure and relationships among distinct data processing steps, can be applied to a systematic exploration of the undular bores having different values of h_1/h_0 and propagating on sloping beaches with distinct slopes.

Nomenclature

Term	Definition
A_c	$(=A_{c1} + A_{c2})$, convective acceleration (LT^{-2})
A_{c1}	$(=u\partial u/\partial x)$, 1st convective acceleration (LT^{-2})
A_{c2}	$(=v\partial u/\partial y)$, 2nd convective acceleration (LT^{-2})
A_l	$(=\partial u/\partial t)$, local acceleration (LT^{-2})
A_t	$(=A_l + A_{c1} + A_{c2})$, total acceleration (LT^{-2})
D_r	relative deviation (-)
f	frequency (T^{-1})
f_{fd}	frequency demarcation (T^{-1})
F_{r0}	$(=U_{bf}/(gh_0)^{1/2})$, Froude number (-)
g	gravity acceleration (LT^{-2})
h_0	downstream still water depth (L)
h_1	upstream still water depth (L)
h_p	potential associated with gravitational force (L)
k	(with $k \geq 5$), order of leading wave (-)
n	$(=1–4)$, order of leading wave (-)
p	pressure $(ML^{-1}T^{-2})$
P	$(=(1/\rho)\partial p/\partial x)$, pressure gradient divided by density (LT^{-2})
S_0	slope of sloping beach (-)
t	time defined relative position of crest of 1st leading wave from toe of sloping beach (T)
t'	time defined with respect to gate opening initially (T)
t_s	specified time (T)
u	ensemble-averaged horizontal velocity (LT^{-1})
U_{bf}	bore front velocity (LT^{-1})
u_u	uniform horizontal velocity in external stream (LT^{-1})
v	ensemble-averaged vertical velocity (LT^{-1})
x	horizontal onshore distance with $x = 0$ located at toe of sloping beach (L)
x_{bpn}	breaking point of nth leading wave in x direction $(n = 1–4)$ (L)
x_{Rmax}	position of maximum run-up height at x direction (L)
x_{SMS}	$(=194.0$ cm), position of specified measuring section in x direction (L)
x_{sws}	$(=180.0$ cm), position of still-water-shoreline in x direction (L)

y	vertical upward distance measured from horizontal bottom (L)
y'	($=y-x/20$), a translated ordinate used to mark height above beach surface (L)
Δt	time interval (T)
$\Delta t_{framing}$	time elapse between two consecutive images taken by high-speed camera at specified framing rate (T)
Δx	spatial interval (L)
μ	dynamic viscosity (ML^{-1}T^{-1})
ρ	fluid density (ML^{-3})
η	free surface elevation with reference to h_0 (L)
η'	free surface elevation with reference to beach surface (L)
η_{fb}	freeboard of free surface elevation (L)
$(\dots)^*$	variable in dimensionless form
$(\dots)_{max}$	maximum value of a physical quantity
$[\dots]_{gb}$	physical quantity of generated bore
$[\dots]_{lw}$	physical quantity of leading wave
$[\dots]_{pb}$	physical quantity of pure bore
$\{\dots\}_{pda}$	partially depth-averaged value of physical quantity

Appendix A Decomposition of Free Surface Elevation Using FFT and IFFT

Using the peak-to-peak or trough-to-trough counting method, the periods and frequencies of the leading waves can be determined directly from the time series of ensemble-averaged free surface elevation of the generated bore $[\eta'(t)]_{gb}$ at the SMS ($x = x_{SMS}$ =194.0 cm). As seen in Figure 4, they vary approximately from 0.25 to 0.50 s and from 2.00 to 4.00 Hz. In addition, the characteristic time and frequency scales of the long-wave-featured pure bore are estimated to be around 10.00–15.00 s and 0.067–0.10 Hz approximately, much lower than those of the leading waves. Note that the time series of the free surface elevation of the generated bore is, in fact, a temporally transient, non-stationary signal. If the temporal variation of frequency underlying such a signal is considered to be the target of interest, it would be better to use Hilbert–Huang Transform or Wavelet Transform for further study. However, the topic is outside the scope of the present study. The main concern herein is to separate the time series of the generated bore into the counterparts of the pure bore and leading waves by taking advantage of their very distinct frequency contents. Under such a situation, it would be convenient to utilize the FFT and IFFT techniques for achieving this goal.

Using FFT, the power spectrum $S(f)$ of the ensemble-averaged free surface elevation of the generated bore at the SMS is obtained and shown in Figure A1a with a frequency resolution $\Delta f = 0.0337$ Hz. Due to each leading wave behaving like a transient wave but not a periodical wave, absence of prominent spectral peak at the corresponding frequency of each leading wave is clearly evidenced in Figure A1a. Most energy is distributed over relatively low frequency range, say $f <$ (0.606–0.908) Hz, revealing main contribution from the pure bore. As generally expected for a nonlinear free surface disturbance, the higher harmonics and lower subharmonics (Lin [34]) of the pure bore exist in the spectrum for 0.0337 Hz $< f \le$ 0.908 Hz approximately (at least with five higher harmonics). In addition, the counterparts for the leading waves range about from 0.606 to 9.032 Hz, thus leading to the combined contribution from the pure bore and leading waves for 0.606 Hz $\le f \le$ 0.908 Hz. Herein, a frequency demarcation $f = f_{fd} = 0.707$ Hz is first identified to separate the free surface elevation of generated bore into the counterparts of pure bore for $f < f_{fd}$ and leading waves for $f > f_{fd}$.

Applying IFFT to the amplitude spectrum of $[\eta'(t)]_{gb}$ with $f_{fd} = 0.707$ Hz, the time series of free surface elevation for the pure bore are presented in Figure A1b. Only the time series of free surface elevation for 0 s $\le t \le$ 7.0 s is shown for easy comparison (the counterparts for 7.0 s $\le t \le$ 13.0 s before and after performing IFFT are totally identical due to absence of the leading waves). It is also interestingly found that, if f_{fd} is designated to be 0.606, 0.740, 0.807, or 0.908 Hz, discernable difference between the corresponding free surface elevation of pure bore and that for $f_{fd} = 0.707$ Hz is hardly observed in Figure A1b. Especially, the free surface elevations of the pure bore for $f_{fd} = 0.707$ and 0.740 Hz are almost identical. This is because the ratios of the energy underlying the power spectrum between 0.606 Hz $\le f \le$ 0.707 (or 0.740) Hz and 0.707 (or 0.740) Hz $\le f \le$ 0.908 Hz to the counterpart between 0.0337 Hz $\le f \le$ 0.707 Hz is as small as 0.15% (or 0.23%) and 0.18% (or 0.11%), respectively. The results strongly demonstrate almost no influence on the separation of the free surface elevation not only for 0.707 Hz $\le f \le$ 0.740 Hz but also for 0.606 Hz $\le f \le$ 0.908 Hz. However, for $f_{fd} \ge$ 0.9754 Hz or $f_{fd} \le$ 0.539 Hz, more prominent deviation of the free surface elevation of the pure bore takes place with respect to that for $f_{fd} = 0.707$ (or 0.740) Hz, eventually leading to inappropriate separation of the free surface (not shown).
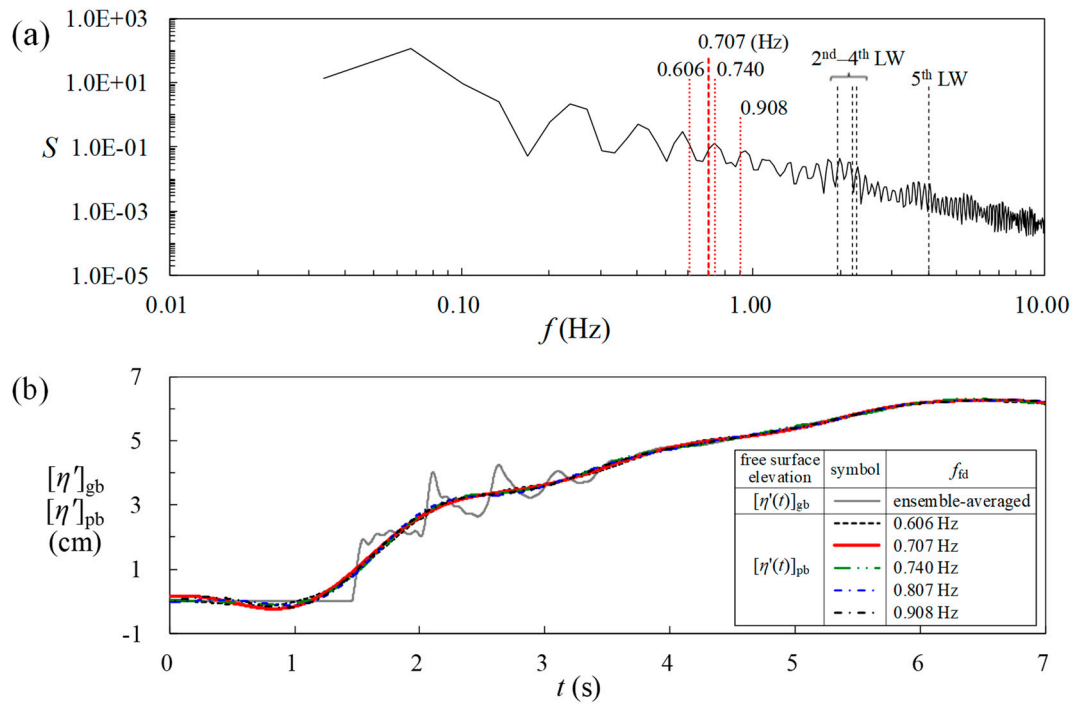
Figure A1. (**a**) Power spectrum $S(f)$ of free surface elevation $[\eta'(t)]_{gb}$ measured at SMS; (**b**) obtaining free surface elevation of pure bore $[\eta'(t)]_{pb}$ from counterpart of pure bore $[\eta'(t)]_{gb}$ using inverse fast Fourier transform (IFFT) with five different values of f_{fd}.

Appendix B Details for Calculation of Accelerations and Relative Deviations
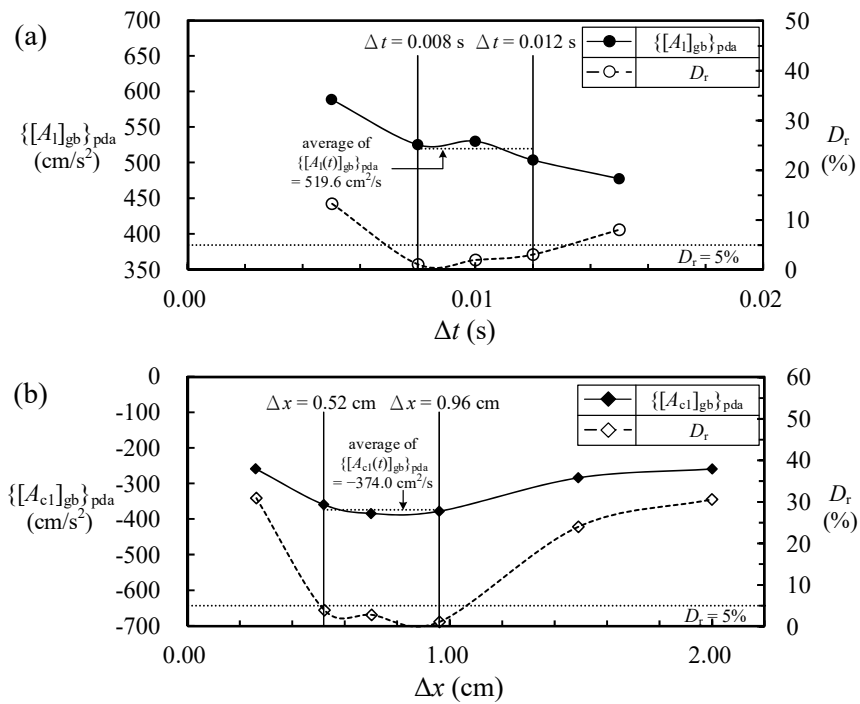

Figure A2. Computed results and relative deviations for values of (**a**) local acceleration $\{[A_l]_{gb}\}_{pda}$; and (**b**) first convective acceleration $\{[A_{cl}]_{gb}\}_{pda}$ at $t = 2.069$ s. Promising range of Δt or Δx, within which relative deviation D_r of each result of either $\{[A_l]_{gb}\}_{pda}$ or $\{[A_{cl}]_{gb}\}_{pda}$ varies only within 4.0% with reference to conditional average, is marked between two vertical lines.

Table A1. List of velocity data at different times and calculation of local acceleration $[A_1(y')]_{gb}$ for $t = 2.069$ s with five different time intervals. Note that partially depth-averaged values of local acceleration $\{[A_1]_{gb}\}_{pda}$ and their relative deviations D_r are addressed at the bottom of the table.

(1)	(2)	(3)	(4)	(5)	(6)	(7)	(8)	(9)
y' (cm)	$[u(y', t-\Delta t)]_{gb}$ (cm/s) $t-\Delta t = 2.059$ s	$[u(y', t)]_{gb}$ (cm/s) $t = 2.069$ s	$[u(y', t+\Delta t)]_{gb}$ (cm/s) $t+\Delta t = 2.079$ s	$[A_1(y')]_{gb}$ (cm/s^2) $\Delta t = 0.005$ s	$[A_1(y')]_{gb}$ (cm/s^2) $\Delta t = 0.008$ s	$[A_1(y')]_{gb}$ (cm/s^2) $\Delta t = 0.010$ s	$[A_1(y'')]_{gb}$ (cm/s^2) $\Delta t = 0.012$ s	$[A_1(y')]_{gb}$ (cm/s^2) $\Delta t = 0.015$ s
3.140			72.86					
3.053			72.86					
2.966			72.86					
2.878			72.86					
2.791			72.86					
2.704		67.52	72.86	578.4	441.5	533.8	452.5	459.9
2.617		67.85	72.86	512.4	400.3	500.8	425.0	437.9
2.530		67.66	72.86	550.8	424.3	520.0	441.0	445.8
2.442		67.05	72.86	718.2	500.8	581.2	492.0	468.1
2.355	60.52	66.67	72.86	718.2	548.4	617.1	523.7	498.7
2.268	60.52	66.67	72.86	718.2	628.4	617.1	574.2	509.6
2.181	60.52	66.67	72.86	744.8	628.4	617.1	574.2	564.5
2.093	60.52	66.67	73.56	764.3	673.8	652.0	593.0	572.6
2.006	60.52	66.67	73.65	760.9	721.8	656.3	599.0	575.7
1.919	60.52	66.67	73.74	759.4	695.5	661.2	589.2	576.0
1.832	60.52	66.67	73.60	751.7	660.1	654.2	581.8	559.9
1.745	60.52	66.91	73.28	730.8	612.7	637.8	583.6	539.2
1.657	60.85	67.28	72.92	716.4	574.2	603.5	568.7	521.5
1.570	61.35	67.40	72.61	676.1	569.4	563.2	546.3	498.1
1.483	61.63	67.38	72.28	627.7	545.8	532.4	520.6	486.3
1.396	61.87	66.85	71.69	564.8	521.9	491.3	502.7	474.9
1.308	62.17	66.41	71.06	511.2	500.1	444.5	486.8	457.0
1.221	62.14	65.81	70.57	462.2	478.5	421.6	475.8	439.6
1.134	61.94	65.13	69.84	423.5	454.5	395.0	451.9	426.4
1.047	61.55	64.61	69.30	416.9	437.9	387.4	445.7	414.1
0.960	61.02	64.17	68.97	383.0	403.8	397.4	427.5	402.7
0.872	60.21	63.84	68.63	345.8	403.4	421.1	417.9	388.4
0.785	59.62	63.55	67.89	351.3	390.6	413.4	409.1	378.5
0.698	58.91	62.87	66.94	343.3	387.1	401.6	404.4	361.3
0.611	58.05	62.04	65.60					
0.523	57.08	61.00	64.10					
0.436	55.79	59.61	62.25					
0.349	51.76	55.30	57.66			boundary layer (not included)		
0.262	45.14	46.61	47.89					
0.174	38.90	38.12	38.55					
0.087	33.12	30.26	29.84					
0.000	0.00	0.00	0.00					
				$\{[A_1]_{gb}\}_{pda}$ (cm/s^2)				
				588.8	525.1	530.0	503.6	477.4
	average determined from the values of $\{[A_1]_{gb}\}_{pda}$ for $\Delta t = 0.008, 0.010$, and 0.012 s					D_r (%)		
	519.6 (cm/s^2)			13.3	1.1	2.0	3.1	8.1

Table A2. List of velocity data at different sections for $t = 2.069$ s and calculation of first convective acceleration $[A_{c1}(y')]_{gb}$ for $t = 2.069$ s with six different spatial intervals. Note that partially depth-averaged values of first convective acceleration $\{[A_{cl}]_{gb}\}_{pda}$ and their relative deviations D_r are presented at the bottom of the table.

(1)	(2)	(3)	(4)	(5)	(6)	(7)	(8)	(9)	(10)
y' (cm)	$[u(x-\Delta x, y')]_{gb}$ (cm/s) $x-\Delta x = 193.04$ cm	$[u(x, y')]_{gb}$ (cm/s) $x = 194.00$ cm	$[u(x+\Delta x, y')]_{gb}$ (cm/s) $x+\Delta x = 194.96$ cm	$[A_{c1}(y')]_{gb}$ (cm/s²) $\Delta x = 0.26$ cm	$[A_{c1}(y')]_{gb}$ (cm/s²) $\Delta x = 0.52$ cm	$[A_{c1}(y')]_{gb}$ (cm/s²) $\Delta x = 0.70$ cm	$[A_{c1}(y')]_{gb}$ (cm/s²) $\Delta x = 0.96$ cm	$[A_{c1}(y')]_{gb}$ (cm/s²) $\Delta x = 1.49$ cm	$[A_{c1}(y')]_{gb}$ (cm/s²) $\Delta x = 2.0$ cm
3.140									
3.053	73.32								
2.966	73.32								
2.878	73.32								
2.791	73.32								
2.704	73.32	67.52		317.3	−318.8	−425.2	−407.4	−137.7	−256.5
2.617	73.32	67.85		−187.3	−278.1	−395.3	−386.0	−145.3	−246.7
2.530	73.32	67.66		−186.7	−429.9	−412.8	−398.5	−182.4	−268.3
2.442	73.32	67.05	58.84	−185.1	−425.3	−463.0	−505.6	−238.7	−299.8
2.355	73.32	66.67	59.55	−189.8	−422.4	−460.4	−477.9	−322.0	−314.9
2.268	73.32	66.67	60.09	−211.6	−422.4	−460.4	−459.4	−324.7	−286.5
2.181	73.32	66.67	60.39	−239.4	−422.4	−460.4	−448.8	−324.5	−284.4
2.093	73.24	66.67	60.60	−284.7	−422.4	−460.4	−438.8	−308.6	−286.1
2.006	73.39	66.67	60.62	−342.2	−442.4	−476.7	−443.6	−317.6	−284.7
1.919	73.52	66.67	60.74	−405.1	−455.1	−488.1	−443.6	−328.7	−284.3
1.832	73.30	66.67	60.71	−374.3	−435.3	−480.4	−437.1	−340.6	−288.0
1.745	73.01	66.91	60.52	−377.3	−451.4	−483.0	−435.2	−356.5	−288.8
1.657	72.74	67.28	60.56	−408.3	−481.1	−491.2	−426.7	−361.4	−283.5
1.570	72.55	67.40	60.53	−422.0	−458.4	−461.7	−422.3	−356.8	−277.9
1.483	72.13	67.38	60.30	−433.7	−467.1	−454.2	−415.3	−344.7	−258.6
1.396	71.79	66.85	60.32	−418.7	−425.2	−427.9	−399.3	−333.8	−240.7
1.308	71.35	66.41	60.65	−403.1	−382.8	−385.5	−370.1	−316.2	−227.9
1.221	70.86	65.81	60.85	−375.6	−335.1	−335.8	−342.9	−301.8	−218.8
1.134	70.21	65.13	61.05	−340.5	−301.7	−299.2	−310.7	−283.4	−214.4
1.047	69.24	64.61	61.08	−270.6	−226.9	−238.9	−274.7	−265.2	−217.3
0.960	68.28	64.17	61.14	−198.5	−199.9	−197.0	−238.6	−248.3	−220.3
0.872	67.50	63.84	60.91	−120.5	−157.8	−166.3	−219.0	−236.1	−223.7
0.785	66.72	63.55	60.73	−69.3	−129.4	−146.8	−198.2	−231.1	−226.9
0.698	65.53	62.87	60.11	−79.9	−136.1	−153.4	−177.5	−217.5	−228.7
0.611	64.59	62.04	59.42						
0.523	63.66	61.00	58.21						
0.436	62.46	59.61	55.98						
0.349	59.63	55.30	47.93			boundary layer (not included)			
0.262	54.40	46.61	41.13						
0.174	46.51	38.12	34.53						
0.087	38.62	30.26	28.31						
0.000	31.13	0.00	0.00						
						$\{[A_{cl}]_{gb}\}_{pda}$ (cm/s²)			
				−258.6	−359.5	−384.3	−378.2	−284.3	−259.5
	expected average estimated from the values of $\{[A_{cl}]_{gb}\}_{pda}$ for $\Delta x = 0.52$, 0.70 and 0.96 cm −374.0 (cm/s²)					D_r (%)			
				30.9	3.9	2.8	1.1	24.0	30.6

Table A3. List of velocity data for $t = 2.069$ s and calculation of second convective acceleration $[A_{c2}(y')]_{gb}$, $[A_t(y')]_{gb}$ and $[P(y')]_{gb}$ $(=[(1/\rho)\partial p(y')/\partial x]_{gb})$. Note that partially depth-averaged values for $\{[A_{c2}]_{gb}\}_{pda}$, $\{[A_t]_{gb}\}_{pda}$ and $\{[P]_{gb}\}_{pda}$ are all shown at the bottom of the table.

(1)	(2)	(3)	(4)	(5)	(6)
y' (cm)	$[v(y')]_{gb}$ (cm/s) $x = 194.00$ cm	$[u(y')]_{gb}$ (cm/s) $x = 194.00$ cm	$[A_{c2}(y')]_{gb}$ (cm/s^2)	$[A_t(y')]_{gb}$ (cm/s^2)	$[P(y')]_{gb}$ (cm/s^2)
3.140					
3.053					
2.966					
2.878					
2.791					
2.704	14.57	67.52	−55.2	71.3	−71.3
2.617	14.20	67.85	−11.2	103.5	−103.5
2.530	15.36	67.66	70.8	192.3	−192.3
2.442	12.19	67.05	69.4	144.9	−144.9
2.355	12.10	66.67	26.4	165.6	−165.6
2.268	11.33	66.67	0.0	157.7	−157.7
2.181	11.18	66.67	0.0	168.4	−168.4
2.093	11.20	66.67	0.0	213.2	−213.2
2.006	11.35	66.67	0.0	212.7	−212.7
1.919	11.46	66.67	0.0	217.6	−217.6
1.832	11.41	66.67	−15.7	201.4	−201.4
1.745	11.24	66.91	−39.1	163.4	−163.4
1.657	10.69	67.28	−30.1	146.7	−146.7
1.570	10.22	67.40	-6.0	134.9	−134.9
1.483	10.11	67.38	31.8	148.9	−148.9
1.396	9.15	66.85	50.8	142.7	−142.7
1.308	7.86	66.41	47.0	121.4	−121.4
1.221	8.03	65.81	59.0	137.7	−137.7
1.134	7.29	65.13	50.1	134.3	−134.3
1.047	6.35	64.61	35.0	147.6	−147.6
0.960	5.71	64.17	25.2	184.0	−184.0
0.872	4.98	63.84	17.6	219.7	−219.7
0.785	5.41	63.55	30.1	245.4	−245.4
0.698	4.94	62.87	42.7	266.9	−266.9
0.611	5.26	62.04			
0.523	4.21	61.00			
0.436	3.85	59.61			
0.349	3.15	55.30		boundary layer (not included)	
0.262	2.54	46.61			
0.174	1.02	38.12			
0.087	0.46	30.26			
0.000	0.00	0.00			
			$\{[A_{c2}]_{gb}\}_{pda}$ (cm/s^2)	$\{[A_t]_{gb}\}_{pda}$ (cm/s^2)	$\{[P]_{gb}\}_{pda}$ (cm/s^2)
			16.6	168.4	−168.4

References

1. Grue, J.; Pelinovsky, E.N.; Frustus, D.; Talipova, T.; Kharif, C. Formation of undular bores and solitary waves in the Strait of Malacca caused by the 26 December 2004 Indian Ocean Tsunami. *J. Geophys. Res.* **2008**, *113*, C005008. [CrossRef]
2. Lin, C.; Kao, M.J.; Wong, W.Y.; Shao, Y.P.; Hu, C.F.; Yuan, J.M.; Raikar, R.V. Effect of leading waves on velocity distribution of undular bore traveling over sloping bottom. *Eur. J. Mech. B Fluids* **2019**, *73*, 75–99. [CrossRef]
3. Yeh, H.H.; Ghazali, A. On bore collapse. *J. Geophys. Res.* **1988**, *93*, 6930–6936. [CrossRef]

4.   Yeh, H.H.; Ghazali, A.; Marton, I. Experimental study of bore run-up. *J. Fluid Mech.* **1989**, *206*, 563–578. [CrossRef]

5.   Shimozono, T. Experimental study on boundary layer flow under undular and turbulent bores. *Proc. Coast. Eng. Conf. B2 JSCE* **2011**, *67*, 46–50. (In Japanese) [CrossRef]

6.   Peregrine, D.H. Calculations of the developments of an undular bore. *J. Fluid Mech.* **1966**, *25*, 312–330. [CrossRef]

7.   Soares Frazao, S.; Zech, Y. Undular bores and secondary waves-Experiments and hybrid finite-volume modelling. *J. Hydraul. Res.* **2014**, *40*, 33–43. [CrossRef]

8.   Gavrilyuk, S.; Liapidevskii, V.; Chesnokov, A. Spilling breakers in shallow water: Applications to Favre waves and to the shoaling and breaking of solitary waves. *J. Fluid Mech.* **2016**, *808*, 441–468. [CrossRef]

9.   Kharif, C.; Abid, M. Nonlinear water waves in shallow water in the presence of constant vorticity: A Whitham approach. *Eur. J. Mech. B Fluids* **2018**, *72*, 12–22. [CrossRef]

10. Madsen, P.A.; Svendsen, I.A. Turbulence bores and hydraulic jumps. *J. Fluid Mech.* **1983**, *129*, 1–25. [CrossRef]

11. Favre, H. *Etude Theorique et Experimentale des Ondes de Translation Dans les Canaux Decouverts*; Dunod: Paris, France, 1935.

12. Treske, A. Undular bores (Favre-waves) in open channels: Experimental studies. *J. Hydraul. Res.* **1994**, *32*, 335–370. [CrossRef]

13. Stansby, P.K.; Chegini, A.; Barnes, T.C.D. The initial stages of dam-break flow. *J. Fluid Mech.* **1998**, *374*, 407–424. [CrossRef]

14. Ho, D.V.; Meyer, R.E. Climb of a bore on a beach—Part 1. Uniform beach slope. *J. Fluid Mech.* **1962**, *14*, 305–318. [CrossRef]

15. Shen, M.C.; Meyer, R.E. Climb of a bore on a beach—Part 2. Non-uniform beach slope. *J. Fluid Mech.* **1963**, *16*, 108–112. [CrossRef]

16. Shen, M.C.; Meyer, R.E. Climb of a bore on a beach—Part 3. Run up. *J. Fluid Mech.* **1963**, *16*, 113–125. [CrossRef]

17. Packwood, A.R. Surf and Run-Up on Beaches. Ph.D. Thesis, Bristol University, Bristol, UK, 1980.

18. Guard, P.A.; Baldock, T.E. The influence of seaward boundary conditions on swash zone hydrodynamics. *Coast. Eng.* **2007**, *54*, 321–331. [CrossRef]

19. Zhang, Q.; Liu, P.L.F. A numerical study of swash flows generated by bores. *Coast. Eng.* **2008**, *55*, 1113–1134. [CrossRef]

20. Miller, R.L. Experimental determination of run-up of undular and fully developed bores. *J. Geophys. Res.* **1968**, *73*, 4497–4510. [CrossRef]

21. Yeh, H.H. Tsunami bore run-up. *Nat. Hazards* **1991**, *4*, 209–220. [CrossRef]

22. Barnes, M.P.; O'Dongoghue, T.; Alsina, J.M.; Baldock, T.E. Direct bed shear stress measurements in bore-driven swash. *Coast. Eng.* **2009**, *56*, 853–867. [CrossRef]

23. O'Donoghue, T.; Pokrajac, D.; Hondebrink, L.J. Laboratory and numerical study of dambreak-generated swash on impermeable slopes. *Coast. Eng.* **2010**, *57*, 513–530. [CrossRef]

24. Kikkert, G.A.; O'Donoghue, T.; Pokrajac, D.; Dodd, N. Experimental study of boredriven swash hydrodynamics on impermeable rough slopes. *Coast. Eng.* **2012**, *60*, 149–166. [CrossRef]

25. Jensen, A.; Pedersen, G.K.; Wood, D.J. An experimental study of wave run-up at a steep beach. *J. Fluid Mech.* **2003**, *486*, 161–188. [CrossRef]

26. Puleo, J.A.; Farhadzadeh, A.; Kobayashi, N. Numerical simulation of swash zone fluid accelerations. *J. Geophys. Res.* **2007**, *112*, C07007. [CrossRef]

27. Higuera, P.; Liu, P.L.F.; Lin, C.; Wong, W.Y.; Kao, M.J. Laboratory-scale swash flows generated by a non-breaking solitary wave on a steep slope. *J. Fluid Mech.* **2018**, *847*, 186–227. [CrossRef]

28. Chang, K.A.; Liu, P.L.F. Velocity, acceleration and vorticity under a breaking wave. *Phys. Fluids* **1998**, *10*, 327–329. [CrossRef]

29. Jensen, A.; Sveen, J.K.; Grue, J.; Richon, J.B.; Gray, C. Acceleration in water waves by extended particle image velocimetry. *Exp. Fluids* **2001**, *30*, 500–510. [CrossRef]

30. Pedrozo-Acuna, A.; Alegria-Arzaburu, A.R.; Torres-Freyermuth, A.; Mendoza, E.; Silva, R. Laboratory investigation of pressure gradients induced by plunging breakers. *Coast. Eng.* **2011**, *58*, 722–738. [CrossRef]

31. Lin, C.; Wong, W.Y.; Raikar, R.V.; Hwung, H.H.; Tsai, C.P. Characteristics of accelerations and pressure gradient during run-down of solitary wave over very steep beach—A case study. *Water* **2019**, *11*, 523. [CrossRef]

32. Tissier, M.; Bonneton, P.; Marche, F.; Chazel, F.; Lannes, D. Nearshore dynamics of tsunami-like undular bores using a fully nonlinear Boussinesq model. *J. Coast. Res.* **2011**, *SI64*, 1–4.

33. Bjørkavag, M.; Kalisch, H. Wave breaking in Boussinesq models for undular bores. *Phys. Lett.* **2011**, *A375*, 1570–1578. [CrossRef]

34. Lin, C. The Characteristics of Internal Flow Field and Bottom Boundary Layer of Waves Propagating on Sloping Bottom. Ph.D. Thesis, Department of Hydraulics and Ocean Engineering, National Cheng Kung University, Tainan, Taiwan, 1989. (In Chinese)